UNIVERSITAT POLITÈCNICA DE CATALUNYA

DEPARTAMENT DE TEORIA DEL SENYAL I COMUNICACIONS

TESI DOCTORAL

HIGHER-ORDER STATISTICS APPLICATIONS IN IMAGE SEQUENCE PROCESSING

AUTOR : ELISA SAYROL CLOLS

DIRECTOR: ANTONI GASULL LLAMPALLAS

UNIVERSITAT POLITÈCNICA DE CATALUNYA

DEPARTAMENT DE TEORIA DEL SENYAL I COMUNICACIONS

TESI DOCTORAL

HIGHER-ORDER STATISTICS APPLICATIONS IN IMAGE SEQUENCE PROCESSING

AUTOR : ELISA SAYROL CLOLS

DIRECTOR: ANTONI GASULL LLAMPALLAS

Barcelona, 27/OCTUBRE/1994

Resum

Aqueta tesi tracta dues aplicacions dels estadístics d'ordre superior al tractament d'imatges.

En primer lloc, es proposa l'ús de mètodes basats en estadístics d'ordre superior per a la restauració d´imatges. Primerament, es consideren imatges degradades per filtres de *blurring* de fase lineal o zero i soroll Gaussià aditiu. S'examina un segon model de degradació per imatges astronòmiques on el blurring es causat per les turbulències de l'atmosfera i les aberracions del telescopi. L'estratègia de restauració en amdós casos es basa en el fet de que la fase del senyal original i la dels seus estadístics d'ordre superior no es ditorsionen per la funció de blurring. Les dificultats associades a combinar senyals de dues dimensions i els seus estadístics d'ordre superior, es redueixen gràcies a la utilització de la transformada de Radon. La projecció a cada angle de la imatge de dues dimensions és un senyal d´una dimensió que pot ser processada per qualsevol mètode de reconstrucció d'una dimensió. En aquesta part de la tesi es desenvolupen mètodes que utilitzen el *Bicepstrum Iterative Reconstruction Algorithm* i el *Weight Slice Algorithm*. Un cop es reconstrueixen les projeccions originals, la transformada inversa de Radon ens dóna la imatge restaurada.

En la segona part de la tesi es proposa una classe de funcions de cost, basades novament en estadístics d'ordre superior, per estimar el vector de moviment entre imatges consecutives d'una sequència. En cas de que les imatges estiguin degradades per soroll Gaussià aditiu de covariància desconeguda, la utilització d'estadístics d'ordre superior és molt apropiada ja que els cumulants de processos Gaussians són nuls. Per a obtenir estimacions consistents es necessiten varies realitzacions de la mateixa sequència, cosa que generalment no és possible. Tanmateix, imatges prèvies de la sequència on el problema d'estimació del moviment ja s'ha resolt, poden ser utilitzades per a obtenir estimacions assimptòticament no esbiaixades. Això es possible quan es pot suposar estacionaritat entre les imatges de la sequència empreades. L'objectiu d'aquesta part del treball d'investigació es l'ús de tècniques basades en estadístics d'ordre superior que puguin estimar moviment fins i tot per a regions o blocs relativament petits. Es defineix també una estimació alternativa quan només es disposa de dues imatges, que supera altres tècniques existents. Finalment es desenvolupa una versió recursiva per casos en què es tingui accés a informació a priori.

Index

Chapter I **Introduction**.....1

1.1 Thesis Outline.....3

1.2 Contributions.....3

Chapter II **HOS in image processing**.....6

2.1 Higher-Order Statistics of Signals.....7

2.1.1 Definitions.....7

2.1.2 Relationship Between Moments and Cumulants.....7

2.1.3 Moments and Cumulants of Stationary Processes..... 11

2.1.4 Polyspectra..... 12

2.1.5 Estimation of HOS..... 13

2.1.6 HOS of Deterministic Signals..... 14

2.1.7 Properties of Moments and Cumulants..... 15

2.1.8 Higher-Order Cepstra..... 18

2.2 HOS in Image Processing..... 19

2.3 General Framework..... 21

Chapter III **Image restoration using HOS**..... 23

3.1 Preliminaries..... 24

3.1.1 The Projection Theorem..... 26

3.1.2 Degradation Model..... 29

3.1.2.1 Noise in Image Systems..... 29

3.1.2.2 Deterministic Blur and Additive Noise Model..... 30

3.1.2.3 Random Blur Model : Turbulence Atmosphere..... 32

3.1.3 HOS-based methods..... 35

3.1.3.1 BIRA..... 35

3.1.3.2 The WS Algorithm 37
3.2 Uniqueness of the Reconstruction from HOS .. 38
3.3 Algorithms 40
3.3.1 Motivation 40
3.3.2 Restoration Scheme 42
3.3.3 Algorithm 1: BIRA-based Reconstruction 43
3.3.4 Algorithm 2: WS-Fourier Phase Reconstruction 45
3.3.5 Algorithm 3: Bispectrum Phase WS Reconstruction ... 47
3.3.5 Computational Complexity 49
3.4 Examples and comparison with other methods. 49
3.5 Conclusions 66

Chapter IV **Image Motion Estimation Using HOS** 67
4.1 Introduction 68
4.1.1 Motion Models 69
4.1.2 A brief review of Motion Estimation Approaches 70
4.1.3 Motivation of the proposed Motion Estimator 72
4.1.4 Problem Formulation 73
4.2 Variance of the DFD 76
4.2.1 Study for Uncorrelated Region and Colored Noise 77
4.2.2 Study for Correlated Region and Colored Noise 81
4.3 Kurtosis of the DFD 83
4.2.1 Study for Uncorrelated Region and Colored Noise 84
4.2.2 Study for Correlated Region and Colored Noise 88
4.4 Modified Kurtosis of the DFD 91
4.4.1 Study for Uncorrelated Region and Colored Noise 91
4.4.2 Study for Correlated Region and Colored Noise 101
4.4.3 Simple Version of the Modified Kurtosis of the DFD. 110

4.5 Recursive Estimation of the Displacement.....110

4.4.1 Recursive Estimation based on the variance of the DFD 110

4.4.2 Recursive Estimation based on the kurtosis of the DFD 111

4.4.1 Recursive Estimation based on the modified kurtosis of the DFD 111

4.6 Conclusions.....115

Chapter V **Conclusions**.....117

4.1 Future Trends.....119

Appendix A 121

Appendix B 123

Appendix C 124

Appendix D 128

References 131

CHAPTER 1

INTRODUCTION

Digital Image Processing is a rapidly evolving field which abundance of applications cover many fields of science and engineering. It is concerned with the treatment and analysis of images or two-dimensional data. Digital image processing can be classified into three subareas: (i) enhancement, restoration and reconstruction, (ii) digitization and compression and (iii) matching, description and recognition. One of the first applications of image processing was conducted in the 1960's and dealt with the restoration of astronomical images that suffered from atmosphere degradations. At that time, the computational burden was prohibitive and ultimate computing facilities could hardly cope with such problem. During the past years, the availability of fast processors and memory at reasonable costs, has permitted to reduce the time of computation and make this branch of engineering widely accessible. Moreover, new applications have been devised as well as new theoretical developments. This technological breakthrough has also allowed the processing of image sequences which add to the 2-D nature of images, a third dimension involving time. An image or video sequence is a series of two-dimensional images sequentially ordered in time. The manipulation of image sequences in areas such as visual communications, multimedia, entertainment, education, medicine, surveillance, remote control and scientific research is constantly growing as the use of video systems is becoming more and more common.

This thesis addresses two topics involving image series, namely image restoration and motion estimation. In both areas we consider that series of images are available, although of different nature in each case.

In the first topic we consider that the image series consist of various versions of the same image that suffered different degradations and spatial shifts. Images corrupted by deterministic or random blur and random noise are studied. We refer to the spatial shift that affects all pixels belonging to a frame in the same way, therefore there is no *intrinsic* movement in the scene. Real examples in this group of image series include, for instance, some type of astronomical images and rigid objects moving in a noisy background.

In the motion estimation problem, the image series are nothing else than image sequences. In this case, a certain scene is been captured and a more complex movement is observed. All pixels may undergo a completely different displacement. There are some situations where the image sequence might be corrupted with noise, for example, images from surveillance cameras or medical images such as echographics with speckle noise.

The objective of image restoration is to remove or at least reduce the effect of degradation *per se*, and thus the original scene is recovered. On the other hand, in motion estimation the prime objective is to obtain the motion that experiences each pixel throughout an image sequence. The final goal may be improvement of the visual quality of the sequence, conversion between video formats or information interpretation. The major challenge in the two studied topics is to solve each particular problem when images have suffered a degradation phenomena. Images acquired are susceptible to be deteriorated by the sensing environment. In general, most images are of very fine quality. Some of them are of lesser quality; and among these a certain subset are of such importance, or are so unique, that is appropriate to consider special techniques by which the degradation is taken into account. Every image of the series suffers a different degradation, however, we may assume that the statistical nature of such degradation does not change along time.

At this point, we might wonder which degradation model best fits our two particular problems; which associated tools are appropriate to solve them; and which is the current state of the art in these fields. Extracting signals from noise, or more generally extracting information of signals from noise is one of the major concerns in engineering. In recent years, Higher-Order Statistics (HOS) of signals techniques have been sucessfully applied to diverse areas of science and engineering such as communications, geophysics, sonar, image processing, radar, oceanography, biomedicine, plasma physics, speech processing and fluid mechanics. It´s poweful properties steem from the large amount of information that HOS of

signals carry as opposed to the limited information of their second-order statistics. Only Gaussian processes are completely specified by second-order statistics. Thus, non-Gaussian processes, that is, many real-world signals, can benefit from the knowledge of their HOS. They are also useful in extracting phase information as well as in detecting the presence of nonlinearities. Moreover, under a broad signal and noise conditions, HOS domains boost the signal-to-noise ratio, allowing an improved detection, parameter estimation and signal reconstruction.

Although it would be natural to first define each of the problems and then find a right solution, we will start introducing Higher-Order Statistics of signals, that given their tedious tractability and multiple properties require a full introductory Chapter. This knowledge will allow the reader to understand properly this work. After this introduction the thesis is developed.

1.1 Thesis Outline

The structure of this thesis is the following. Chapter 2 deals with the definitions and properties of Higher-Order Statistics of signals. Among these we remark the ones more relevant for this work. In contrast to second-order statistics, higher-order statistics are asymptotically unaffected by additive Gaussian disturbances and the phase information is not completely lost, therefore are not phase blind. Literature on recent applications of these techniques to the area of image processing are outlined, including diverse fields such as image restoration, feature extraction, texture analysis and motion estimation. The last part of this chapter presents a general framework for the two problems considered in this thesis. A unique formulation may be given for the two types of image series described in this introduction.

The two following chapters form the burden of the thesis. In Chapter 3 the problem of image restoration is studied. In the first part, the image degradation model is described, including the blur and noise models. The projection theorem that allows the reconstruction of an image from its 1-D projections and 1-D HOS-based reconstruction methods are revisited. In the second part of this chapter, the theoretical bases that allow the reconstruction from either the phase of the Fourier Transform or the phase of the Bispectrum are established. Once all rudiments have been presented, three image restoration algorithms are developed. Several examples obtained by these schemes are shown and discussed in detail.

Chapter 4 deals with the problem of motion estimation. Cost functions based on the variance and kurtosis of the displaced frame difference are reviewed for AR models of the noise and image covariances. Following, a new class of HOS-based cost functions is derived together

with its corresponding recursive version. The improvement of the new strategies with respect to the other cost functions is demonstrated in the examples.

The last chapter of the thesis is devoted to a summary of conclusions of this work. Future trends of research in the area are also suggested.

1.2 Contributions

In this thesis, we find new applications of Higher-Order Statistics to two different image processing topics.

For the image restoration problem we deal with old concepts and new concepts that as a whole contribute to obtain a novel work. First of all, this part deals with old concepts, for example, restoration of images from projections is not new, signal reconstruction from the Fourier phase is not new. However we have thoroughly studied this old concepts and bring about new insights. Thus, the main contributions in this area are summarized in the following points:

- The use of HOS in the area of Image Restoration has just begun to find applicability. In this part of the thesis, the benefits from the properties of HOS in the area are shown.

- We state three Corollaries that are the theoretical bases that guarantee the uniqueness, except for a constant factor, of the reconstruction of image projections when they are degraded by zero-phase blurs or compensated linear phase blurs.

- From the above theoretical results three restoration schemes are developed. Some examples show the improvement for the reconstructed projections and final images.

- New applications of an existing method, the WS algorithm, are demonstrated.

In the second part of the thesis the problem of Image Motion Estimation is considered. The main contributions in this area are the following:

- Analytical expressions of second-order and higher-order cost functions are derived for AR models of the image regions and the noise. The behavior of these functions is obtained and carefully examined.

- A new HOS-based cost function outperforms the previously reported approaches for reasonable small size regions and low SNR. This new approach is based on an adaptive scheme for the estimation of fourth-order cumulants using previous frames.

- We also derive a HOS-based cost function that outperforms a previous fourth-order statistics criterion when only two images of the sequence are available.

- A recursive version of the new cost function to estimate the displacement is presented and compared to the recursive scheme of the second-order cost function.

As a whole, the results of this thesis show some of the possibilities of HOS to image processing.

CHAPTER 2

HIGHER-ORDER STATISTICS IN IMAGE PROCESSING

This chapter presents an overview of the motivation, definitions, properties and applications of Higher-Order Statistics (HOS) to digital image processing. There are four main reasons behind the use of Higher-Order Statistics in signal processing: 1) to suppress additive colored Gaussian noise of unknown power spectrum; 2) to identify non-minimum phase systems or reconstruct non-minimum phase signals; 3) to extract information due to deviations from Gaussianity; and 4) to detect and characterize nonlinear properties in signals or identify nonlinear systems. Image Restoration and Motion Estimation problems are two Image Processing topics that can benefit from these properties. Specifically, for the first problem the first and second property may be applied to reconstruct some type of degraded images, whereas the first and third properties can be utilized to solve the Motion Estimation problem.

Before treating these two particular applications in the following chapters, a review of the definitions and properties of Higher-Order Statistics is presented in the first section of this chapter. General aspects of HOS and particular aspects that best fit our purposes have been included. In section 2, recent developments of HOS to image processing are examined. HOS-based techniques have found applicability to diverse areas such as image restoration, feature extraction, texture analysis and motion estimation. Hence, the motivation of using HOS to the two problems treated in this thesis stems not only from the properties of HOS but from a logical trajectory of recent developments of HOS to image processing. Finally, in the last section, a general framework is introduced for the two problems considered in this thesis. An image restoration model and a motion estimation model are derived from particular cases of a general image model.

2.1 Higher-Order Statistics of signals

The material given in this section was taken from the tutorial papers by Nikias & Raghuveer [1987], Mendel [1991], Nikias & Mendel [1993], and by the recently published book on higher-order statistics by Nikias & Petropulu [1993]. The goal is to provide the basic formulation and properties of HOS in signal processing. Hence, further details and explanations may be found in the above references. For the sake of simplicity, the definitions that follow are given for 1-D signals, although some of them are also derived for 2-D signals.

2.1.1 Definitions

The nth-order moments of a collection of random variables $\boldsymbol{x} = (x_1,x_2,...,x_n)$ are defined as the coefficients of $\omega = (\omega_1,\omega_2,...,\omega_n)$ in the Taylor series expansion (provided it exist) of the moment-generating function:

$$mom(x_1^{k1},x_2^{k2}, ..., x_n^{kn}) = E\{x_1^{k1}x_2^{k2} ... x_n^{kn}\} =$$

$$= (-j)^k \frac{\partial^k \Phi(\omega)}{\partial\omega_1^{k1}\partial\omega_2^{k2} ...\partial\omega_n^{kn}} \Big|_{\omega_1= \omega_2= ...=\omega_n= 0} \qquad (2.1)$$

where

$$\Phi(\omega) = E\{ exp(j\omega^t x) \} \qquad (2.2)$$

is the joint characteristic function and $n = k_1+k_2+...+k_n$. The natural logarithm of (2.2) is the joint second characteristic function [Papoulis, 1984]:

$$\Psi(\omega) = Ln(E\{ exp(j\omega^t x) \})= Ln(\Phi(\omega)) \qquad (2.3)$$

The joint nth-order cumulants are defined as the coefficients of $\omega = (\omega_1,\omega_2,...,\omega_n)$ in the Taylor series expansion of the joint second characteristic function :

$$cum(x_1^{k1},x_2^{k2}, ..., x_n^{kn}) = (-j)^k \frac{\partial^k \Psi(\omega)}{\partial\omega_1^{k1}\partial\omega_2^{k2} ...\partial\omega_n^{kn}} \Big|_{\omega_1= \omega_2= ...=\omega_n= 0} \qquad (2.4)$$

2.1.2 Relationship Between Moments and Cumulants

The general relationship between moments and cumulants of order n is given by [Mendel, 1991]:

$$cum(x_1,x_2, ..., x_n) = \Sigma (-1)^{p-1}(p-1)! E\{\prod_{i\in s_1} x_i\}E\{\prod_{i\in s_2} x_i\}... E\{\prod_{i\in s_p} x_i\} \qquad (2.5)$$

where the summation extends over all partitions $(s_1,s_2,...,s_p)$, $p = 1,2,...,n$, of the set of integers $(1,2,...,n)$. An example that illustrates (2.5) is the following: the set of integers $(1,2,3)$ can be partitioned into :

$p=1$ $\quad s_1 = \{1,2,3\}$

$p=2$ $\quad s_1 = \{1\} \quad s_2 = \{2,3\}$

$\quad s_1 = \{2\} \quad s_2 = \{1,3\}$

$\quad s_1 = \{3\} \quad s_2 = \{1,2\}$

$p=3$ $\quad s_1 = \{1\} \quad s_2 = \{2\} \quad s_3 = \{3\}$

and therefore (2.5) becomes for $n=3$:

$$cum(x_1,x_2,x_3) = E\{x_1x_2x_3\}-E\{x_1\}E\{x_2x_3\}-E\{x_2\}E\{x_1x_3\} - E\{x_3\}E\{x_1x_2\}+2E\{x_1\}E\{x_2\}E\{x_3\} \quad (2.6)$$

which is

$$cum(x_1,x_2,x_3) = E\{x_1x_2x_3\}$$

in the case of zero-mean random variables. Also in this case for the second- and fourth-order cumulants we obtain:

$$cum(x_1,x_2) = E\{x_1x_2\}$$

$$cum(x_1,x_2,x_3,x_4)=E\{x_1x_2x_3x_4\}-E\{x_1x_2\}E\{x_3x_4\}-E\{x_1x_3\}E\{x_2x_4\}-E\{x_1x_4\}E\{x_2x_3\} \quad (2.7)$$

The relationship expressed in (2.5) implies that the computation of cumulants of order n requires knowledge of all moments up to order n whether the signal is zero-mean or not. This is easily seen in (2.6) and (2.7). We also observe that second- and third-order moments and second- and third-order cumulants are identical for zero-mean random variables, whereas this is not true for higher than third-order statistics.

Example 2.1

The moments

$$m_1 = mom(x_1) = E\{x_1\} \qquad m_2 = mom(x_1,x_1) = E\{x_1^2\}$$

$$m_3 = mom(x_1,x_1,x_1)= E\{x_1^3\} \qquad m_4 = mom(x_1,x_1,x_1,x_1) = E\{x_1^4\}$$

of the random variable $\{x_1\}$are related to its cumulants by :

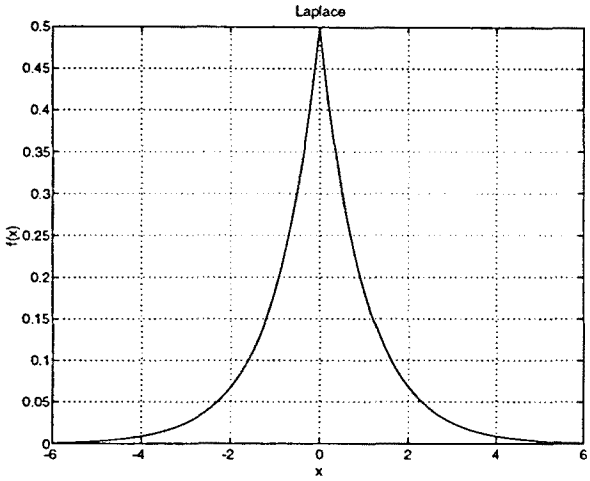

$f(x) = 0.5 \exp(-|x|)$

n	m_n	c_n
1	0	0
2	2	2
3	0	0
4	24	12

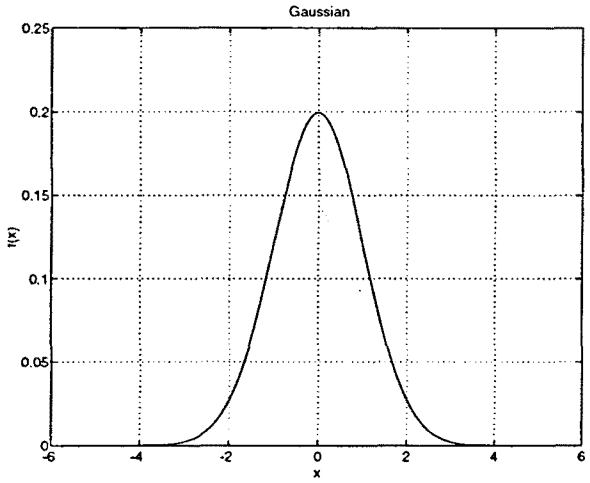

$f(x) = 0.5 \exp\{\frac{-x^2}{2\sigma^2}\} / (2\pi\sigma^2)^{1/2}$

n	m_n	c_n
1	0	0
2	σ^2	σ^2
3	0	0
4	$3\sigma^4$	0

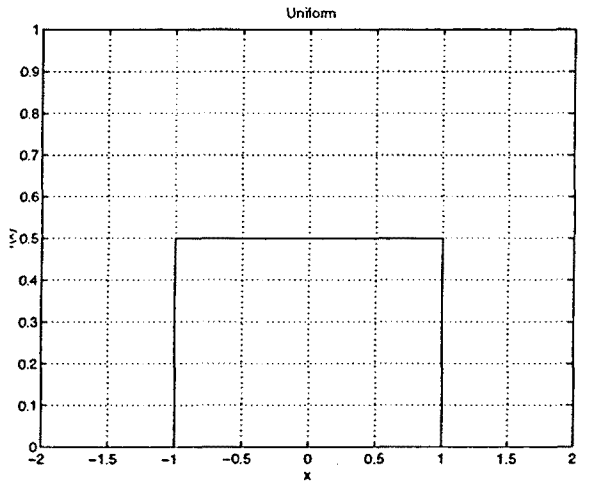

$f(x) = \frac{1}{2c} \quad -c \le x \le +c$

n	m_n	c_n
1	0	0
2	$c^2/3$	$c^2/3$
3	0	0
4	$c^4/5$	$-2c^4/15$

Figure 2.1 The *n*th-order moments and cumulants for *n=1,2,3,4* of the Laplacian, Gaussian *(σ = 1)* and Uniform *(c=1)* Probability Density Functions (pdfs).

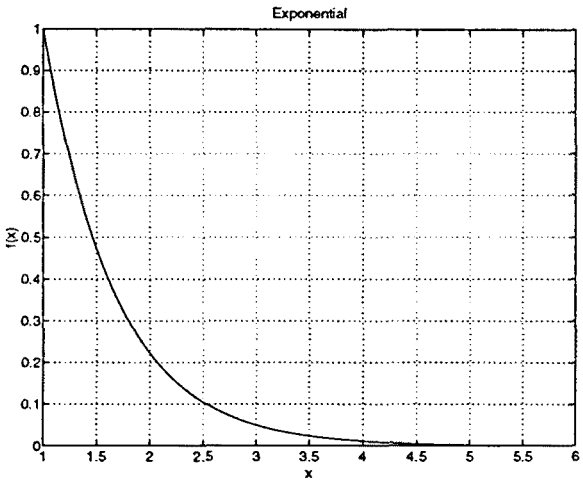

$$f(x) = \exp(-\lambda x)\, u(x)$$

n	m_n	c_n
1	$\frac{1}{\lambda}$	$\frac{1}{\lambda}$
2	$\frac{2}{\lambda^2}$	$\frac{1}{\lambda^2}$
3	$\frac{6}{\lambda^3}$	$\frac{2}{\lambda^3}$
4	$\frac{24}{\lambda^4}$	$\frac{6}{\lambda^4}$

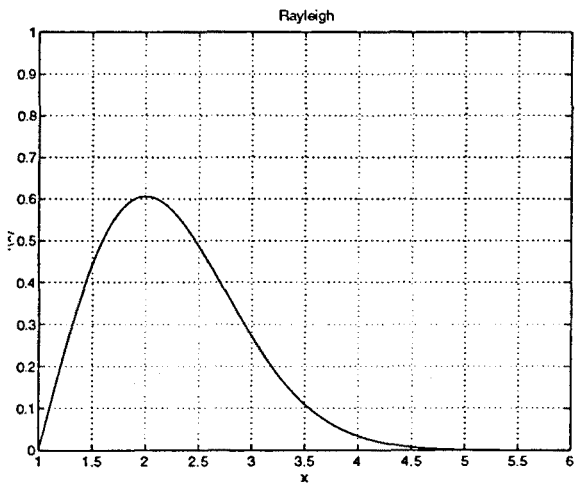

$$f(x) = \exp\{\frac{-x^2}{2\alpha^2}\}\frac{x}{\alpha^2}u(x)$$

n	m_n	c_n
1	$\alpha(\pi/2)^{1/2}$	$\alpha(\pi/2)^{1/2}$
2	$2\alpha^2$	$(2-\pi/2)\alpha^2$
3	$3\alpha^3(\pi/2)^{1/2}$	$-3\alpha^3\pi(\pi/2)^{1/2}$
4	$8\alpha^4$	$1/2\alpha^4(12\pi-3\pi^2-8)$

Figure 2.2 The *n*th-order moments and cumulants for *n=1,2,3,4* of the Exponential *(λ = -1.5)* and Rayleigh *(α= -1.5)* Probability Density Functions (pdfs).

$$\gamma_1^x = c_1 = cum(x_1) = m_1 \qquad \gamma_2^x = c_2 = cum(x_1,x_1) = m_2 - m_1^2$$

$$\gamma_3^x = c_3 = cum(x_1,x_1,x_1) = m_3 - 3m_2m_1 + 2m_1^3$$

$$\gamma_4^x = c_4 = cum(x_1,x_1,x_1,x_1) = m_4 - 4m_3m_1 - 3m_2^2 + 12m_2m_1^2 - 6m_1^4 \qquad (2.8)$$

If $m_1 = 0$ it follows that $\gamma_2^x = c_2 = m_2$, $\gamma_3^x = c_3 = m_3$ and $\gamma_4^x = c_4 = m_4 - 3m_2^2$. Figure. 2.1 and 2.2 show the moments and cumulants up to fourth-order for different Probability Density Functions *(pdf)*. We observe that symmetrically distributed *pdfs* have odd-order statistics identically zero.

Moreover, for the Gaussian distribution we observe that the fourth-order cumulant is zero. In general this is true for all cumulants of order greater than two. However higher-order moments are different from zero.

On the other hand, it is more difficult to infer any conclusion for asymmetric distributions.

2.1.3 Moments and Cumulants of Stationary Processes

Let $\{x(t)\}$ be a real zero-mean stationary process. The nth-order cumulant of $\{x(t)\}$, denoted $C_{n,x}(\tau_1,\tau_2,...,\tau_{n-1})$, is defined as the joint nth-order cumulant of the random variables $\{x(t),x(t+\tau_1)...x(t+\tau_{n-1})\}$, i.e.

$$C_{n,x}(\tau_1,\tau_2,...,\tau_{n-1}) = cum(x(t),x(t+\tau_1),...,x(t+\tau_{n-1})) \qquad (2.9)$$

If $\{x(t)\}$ is non stationary, then the nth-order cumulant explicitly depends on t as well. The second-, third-, and fourth-order cumulants are related to its moments as follows:

$$C_{2,x}(\tau_1) = E\{x(t)x(t+\tau_1)\}$$

$$C_{3,x}(\tau_1,\tau_2) = E\{x(t)x(t+\tau_1)x(t+\tau_2)\}$$

$$\begin{aligned} C_{4,x}(\tau_1,\tau_2,\tau_3) = {} & E\{x(t)x(t+\tau_1)x(t+\tau_2)x(t+\tau_3)\} - \\ & E\{x(t)x(t+\tau_1)\}E\{x(t+\tau_2)x(t+\tau_3)\} - \\ & E\{x(t)x(t+\tau_2)\}E\{x(t+\tau_1)x(t+\tau_3)\} - \\ & E\{x(t)x(t+\tau_3)\}E\{x(t+\tau_1)x(t+\tau_2)\}. \end{aligned} \qquad (2.10)$$

Of course, the second-order cumulant is just the autocorrelation of $x(t)$. By putting $\tau_1 = \tau_2 = \tau_3 = 0$ in (2.10) we get the variance $\gamma_2^x = C_{2,x}(0)$, the skewness $\gamma_3^x = C_{3,x}(0,0)$ and the kurtosis $\gamma_4^x = E\{x^4(t)\} - 3(\gamma_2^x)^2 = C_{4,x}(0,0,0)$ in terms of cumulant lags. The normalized kurtosis is defined as $\gamma_4^x / (\gamma_2^x)^2$.

2.1.4 Polyspectra

Assuming that $C_{n,x}(\tau_1,\tau_2,...,\tau_{n-1})$ is absolutely summable, the nth-order polyspectrum is defined as the $(n-1)$-dimensional discrete-time Fourier transform of the nth-order cumulant, i.e.,

$$S_{n,x}(\omega_1,\omega_2,...,\omega_{n-1}) = \sum_{\tau_1=-\infty}^{\infty} \cdots \sum_{\tau_{n-1}=-\infty}^{\infty} C_{n,x}(\tau_1,\tau_2,...,\tau_{n-1}) \cdot exp[\, -j \sum_{i=1}^{n-1} \omega_i \tau_i \,] \tag{2.11}$$

The power Spectrum, Bispectrum and Trispectrum are special cases of the nth-order polyspectrum:

Power Spectrum: $n=2$

$$S_{2,x}(\omega) = P_x(\omega) = \sum_{\tau_1=-\infty}^{\infty} C_{2,x}(\tau_1) \cdot exp[\, -j\, \omega_1 \tau_1) \,] \tag{2.12}$$

Bispectrum: $n=3$

$$S_{3,x}(\omega_1,\omega_2) = B_x(\omega_1,\omega_2) = \sum_{\tau_1=-\infty}^{\infty} \sum_{\tau_2=-\infty}^{\infty} C_{3,x}(\tau_1,\tau_2) \cdot exp[\, -j\,(\omega_1\tau_1+\omega_2\tau_2) \,] \tag{2.13}$$

Trispectrum: $n=4$

$$S_{4,x}(\omega_1,\omega_2,\omega_3) = \sum_{\tau_1=-\infty}^{\infty} \sum_{\tau_2=-\infty}^{\infty} C_{4,x}(\tau_1,\tau_2,\tau_3) \cdot exp[\, -j\,(\omega_1\tau_1+\omega_2\tau_2+\omega_3\tau_3) \,] \tag{2.14}$$

Important symmetry conditions, which make the calculations more manageable, exist in the arguments of $C_{n,x}(\tau_1,\tau_2,...,\tau_{n-1})$ and $S_{n,x}(\omega_1,\omega_2,...,\omega_{n-1})$. For example, $C_{3,x}(\tau_1,\tau_2) = C_{3,x}(\tau_2,\tau_1) = C_{3,x}(-\tau_2,\tau_1-\tau_2) = C_{3,x}(-\tau_1,\tau_2-\tau_1) = C_{3,x}(\tau_2-\tau_1,-\tau_1) = C_{3,x}(\tau_1-\tau_2,-\tau_2)$. Using these equations we can divide the (τ_1,τ_2) plane into six symmetry regions for $C_{3,x}$. Knowledge of the cumulants in one of these regions is enough for a complete description of all the plane.

In this thesis, we deal with problems involving random processes added to deterministic signals. For this reason, we are interested in having a definition of the Bispectrum, given in terms of the Fourier Transform of the signal as it is usually done for deterministic signals (see next section). For the bispectrum, the two-frequency index notation is standard, however it hides the three-frequency interaction [Hinich, 1990]. Thus, if x(t) is stationary:

$$E\{X(\omega_1)\,X(\omega_2)\,X(\beta)\}$$

$$= E\{ \sum_{-\infty}^{\infty} \sum_{-\infty}^{\infty} \sum_{-\infty}^{\infty} x(t)x(r)x(h)\, exp[\,-j\,(\omega_1 t+\omega_2 r+\beta h)\,]\ \}$$

$$= \sum_{\tau_1=-\infty}^{\infty} \sum_{\tau_2=-\infty}^{\infty} C_{3,x}(\tau_1,\tau_2)\ exp[\,-j\,(\omega_1\tau_1+\omega_2\tau_2)] \cdot \sum_{t=-\infty}^{\infty} exp[\,-j(\omega_1+\omega_2+\beta)t]$$

$$= S_{3,x}(\omega_1,\omega_2) \cdot \sum_{s=-\infty}^{\infty} \delta((\omega_1+\omega_2+\beta)+2\pi s) \qquad (2.15)$$

where $X(\omega)$ is the Fourier Transform of $\{x(t)\}$, δ is the Dirac delta function and we have applied $r = t+\tau_1$ and $h = t+\tau_2$. For $|w| \le \pi$,

$$E\{X(\omega_1)\,X(\omega_2)\,X(\beta)\} = S_{3,x}(\omega_1,\omega_2) \cdot \delta(\omega_1+\omega_2+\beta) \qquad (2.16)$$

It follows that this expression is different from zero only at $\beta = -\omega_1-\omega_2$. Note that (2.16) is invariant to permutations of the frequency indexes ω_1, ω_2 and $\beta = -\omega_1-\omega_2$, thus, the symmetry regions may be derived. Actually the above relationship holds only for stationary signals. Similarly, by windowing in t, we obtain the Fourier transform of the window $W(\omega)$, instead of the Dirac delta, hence:

$$E\{X(\omega_1)X(\omega_2)X(\beta)\}\,|_{\beta=-\omega_1-\omega_2} = S_{3,x}(\omega_1,\omega_2)W(\omega_1+\omega_2+\beta)\,|_{\beta=-\omega_1-\omega_2} = S_{3,x}(\omega_1,\omega_2)W(0) \qquad (2.17)$$

On the other hand, extensions to the definition of polyspectra for 2-D signals may be easily derived by considering each scalar lag, τ_k or ω_k, as an ordered pair, (τ_{k1},τ_{k2}) or $(\omega_{k1},\omega_{k2})$. Equation (2.11) becomes:

$$S_{n,x}(\omega_{11},\omega_{12};\ldots;\omega_{n-11},\omega_{n-12}) = \sum_{\tau_{11}=-\infty}^{\infty} \ldots \sum_{\tau_{n-12}=-\infty}^{\infty} C_{n,x}(\tau_{11},\tau_{12};\tau_{21},\tau_{22};\ldots;\tau_{n-11},\tau_{n-12})$$

$$\cdot exp[\,-j \sum_{i=1}^{n-1} \omega_{i1}\tau_{i1}+\omega_{i2}\tau_{i2}] \qquad (2.18)$$

2.1.5 Estimation of HOS

In most practical applications, we deal with the problem of estimating the cumulant or moment spectrum of a process when a finite set of observation measurements is available. Actually,

one of the main drawbacks of HOS methods is that, in general, long data records are needed to obtain low variance estimates. Moreover, the computations may be numerically expensive despite the use of fast algorithms. There are two main approaches that can be used to estimate HOS; namely, the conventional (time average and "Fourier" type) and the parametric approach, which is based on autoregressive (AR) moving average (MA), ARMA or Volterra models. The conventional methods, the ones we will use in this thesis and that will be inspected in the following chapters, may be classified in indirect class, direct class and complex demodulates class. See Nikias and Petropulu [1993, Chapter 4] for a thorough review of conventional estimation methods.

2.1.6 HOS of deterministic signals

Let us consider $x(t)$, a real one-dimensional, finite energy, deterministic, discrete-time signal, and assume that its moments, or multiple correlation exist. Then the nth-order moments of energy signals are functions of $(n-1)$-dimensional arguments defined by

$$M_{n,x}(\tau_1,\tau_2,\ldots,\tau_{n-1}) = \sum_{t=-\infty}^{\infty} x(t)\, x(t+\tau_1) \ldots x(t+\tau_{n-1}) \tag{2.19}$$

and their spectra are given by:

$$S_{n,x}(\omega_1,\omega_2,\ldots,\omega_{n-1}) = X(\omega_1)\, X(\omega_2) \ldots X(\omega_{n-1})\; X\Big(-\sum_{k=1}^{n-1}\omega_k\Big) \tag{2.20}$$

It is well known that the Energy Spectrum of $x(t)$, is defined as the Fourier Transform (FT) of its correlation function and is given by

$$P_x(\omega) = X(\omega)\, X^*(\omega), \tag{2.21}$$

where $X(\omega)$ is the Fourier Transform of $x(t)$. In the same way, the Bispectrum $B_x(\omega_1,\omega_2)$ is defined as the Fourier Transform (FT) of its triple correlation function, therefore

$$B_x(\omega_1,\omega_2) = X(\omega_1)\, X(\omega_2) X^*(\omega_1+\omega_2), \tag{2.22}$$

Some authors define the Bispectrum of such a signal as the triple product of the Fourier Transform of the mean subtracted signal. This would bring the definition in line with that of Bispectra of stationary stochastic processes which are defined as the Fourier Transform of third-order cumulant sequences. There are some advantages in using cumulants, instead of moments, with stationary random processes. These are related to ergodicity, testing for statistical independence [Brillinger, 1965], etc. It is not clear if any such advantage is gained with a similar definition when we deal with deterministic signals. Hence, we will proceed

with the definition in Eq. (2.19), as is commonly done in optical applications [Sundaramoorthy, 1990].

For periodic signals the power spectrum is defined as in Eq. (2.19) given the definition of Fourier series with t ranging in one period and dividing by the period of the signal.

We can as well derive similar expressions for 2-D signals. That is, given a discrete $M \times N$ image $x(m,n)$, its nth-order spectrum is defined as:

$$S_{n,x}(\omega_{11},\omega_{12};\ldots;\omega_{n-11},\omega_{n-12}) = X(\omega_{11},\omega_{12}) \ldots X(\omega_{n-11},\omega_{n-12})\, X(-\sum_{k=1}^{n-1}\omega_{k1} - \sum_{k=1}^{n-1}\omega_{k2}) \tag{2.23}$$

where $X(\omega_1,\omega_2)$ is the $M \times N$ DFT of $x(m,n)$.

2.1.7 Properties of Moments and Cumulants

Following are some important properties of moments and cumulants, which are often used in theoretical developments (see [Mendel, 1990] and references therein):

[P1] If λ_i, $i = 1,\ldots,k$ are constants and x_i, $i=1,\ldots,k$, are random variables, then

$$mom(\lambda_1 x_1,\lambda_2 x_2,\ldots,\lambda_n x_n) = \prod_{i=1}^{k}\lambda_i \; mom(x_1,x_2,\ldots,x_n)$$

$$cum(\lambda_1 x_1,\lambda_2 x_2,\ldots,\lambda_n x_n) = \prod_{i=1}^{k}\lambda_i \; cum(x_1,x_2,\ldots,x_n) \tag{2.24a}$$

[P2] Moments and cumulants are symmetric in their arguments, i.e.,

$$mom(x_1,\ldots,x_n) = mom(x_{i1},\ldots,x_{in})$$

$$cum(x_1,\ldots,x_n) = cum(x_{i1},\ldots,x_{in}) \tag{2.24b}$$

where $(i1,\ldots,in)$ is any permutation of $(1,\ldots,n)$.

[P3] If a subset of the n random variables $\{x_i\}$ is independent of the rest, then,

$$cum(x_1,\ldots,x_n) = 0,$$

whereas in general ,

$$mom(x_1,\ldots,x_n) \neq 0. \tag{2.24c}$$

[P4] If the random variables $\{x_i\}$ are independent of the random variables $\{y_i\}$, $i = 1,2,...,n$, then,

$$cum(x_1+y_1,...,x_n+y_n) = cum(x_1,...,x_n)+ cum(y_1,...,y_n) \tag{2.24d}$$

in general this not true for moments, however for the random variables $\{y_0,x_0,x_1,...,x_{n-1}\}$ we have:

$$cum(x_0+y_0,x_1,...,x_n) = cum(x_0,x_1,...,x_n)+cum(y_0,x_1,...,x_n)$$
$$mom(x_0+y_0,x_1,...,x_n) = mom(x_0,x_1,...,x_n)+mom(y_0,x_1,...,x_n) \tag{2.24e}$$

Additional properties that make higher-order statistics very attractive in practical applications may be derived. Next, we summarize some of these important properties with special emphasis to the ones we are going to utilize in this thesis.

1) Deviations from Gaussianity. The nth-order cumulant function of a non-Gaussian stationary random signal can be written as (for $n=3,4$ only) [Mendel, 1991]:

$$C_{n,x}(\tau_1,\tau_2,...,\tau_{n-1}) = E\{x(t)...x(t+\tau_{n-1})\}-E\{g(t)...g(t+\tau_{n-1})\} \tag{2.25}$$

where $g(t)$ is a Gaussian signal that has the same mean value and autocorrelation sequence as $x(t)$. If $x(t)$ is Gaussian then $C_{n,x}(\tau_1,\tau_2,...,\tau_{n-1}) = 0$ for any order. Hence, the cumulants of order greater than two $(n > 2)$, in some sense, measure the non-Gaussian nature of signals.

2) Symmetrically distributed signals. Cumulants of symmetrically distributed signals are zero for odd orders. Therefore we can draw non-symmetrically distributed signals out of symmetrically distributed signals for these orders. Suppose $x(n) = y(n)+v(n)$ where $y(n)$ and $v(n)$ are independent; from property P4 we obtain

$$C_{n,x}(\tau_1,\tau_2,...,\tau_{n-1}) = C_{n,y}(\tau_1,\tau_2,...,\tau_{n-1})+C_{n,v}(\tau_1,\tau_2,...,\tau_{n-1}) \tag{2.26}$$

If $v(n)$ is symmetrically distributed (colored or white) and n>2 and odd, then $C_{n,x}(\tau_1,\tau_2,...,\tau_{n-1}) = C_{n,y}(\tau_1,\tau_2,...,\tau_{n-1})$.

3) Gaussian noise. The cumulants of signals with Gaussian distribution are not only zero for odd orders but for any order n>2. This makes higher-order statistics more robust to additive Gaussian noise than correlation, even if noise is colored. In essence, cumulants can draw non-Gaussian signals out of Gaussian noise for any order n>2.

3) Phase Information. Any higher-order cumulant suppresses linear phase information. Nevertheless, while the power spectrum suppresses all phase information, the Bispectrum does not. Actually we can recover all phase information except for the linear phase

component. This fact makes the Bispectrum useful in identifying non-minimum (mixed) phase systems or sequences. These properties are illustrated in the following example. Let $y(t)$ be the output of a linear time-invariant (LTI) system driven by a non-Gaussian independent, identically distributed (i.i.d.) process, $x(t)$, i.e.,

$$C_{n,x}(\tau_1,\tau_2,\ldots,\tau_{n-1}) = \begin{cases} \gamma_{nx} & \text{if } \tau_1=\tau_2=\ldots,\tau_{n-1}=0 \\ 0 & \text{otherwise} \end{cases} \tag{2.27}$$

where γ_{nx} denotes the nth-order cumulant of $x(t)$. Brillinger and Rosenblatt established that the nth-order cumulant spectra of the input $x(t)$ and the output $y(t)$ are related by:

$$S_{n,y}(\omega_1,\omega_2,\ldots,\omega_{n-1}) = S_{n,x}(\omega_1,\omega_2,\ldots,\omega_{n-1})\, H(\omega_1)\, H(\omega_2) \ldots H(\omega_{n-1})\, H^*\Big(\sum_{k=1}^{n-1}\omega_n\Big)$$

$$= \gamma_{nx}\, H(\omega_1)\, H(\omega_2) \ldots H(\omega_{n-1})\, H^*\Big(\sum_{k=1}^{n-1}\omega_n\Big) \tag{2.28}$$

The Power Spectrum (n=2) is given by:

$$S_{2,y}(\omega_1) = \gamma_{2x}\, |H(\omega_1)|^2 \tag{2.29}$$

where γ_{2x} is the variance of the input white sequence. $S_{2,y}(\omega_1)$ is real and non-negative and we see that all phase information is lost. On the other hand, the Bispectrum (n=3)is written as:

$$S_{3,y}(\tau_1,\tau_2) = \gamma_{3x} H(\omega_1)\, H(\omega_2)\, H^*(\omega_1+\omega_2) \tag{2.30}$$

Its magnitude is given by:

$$|S_{3,y}(\tau_1,\tau_2)| = |\gamma_{3x}|\, |H(\omega_1)|\, |H(\omega_2)|\, |H(\omega_1+\omega_2)| \tag{2.31}$$

whereas the phase information:

$$\psi_y(\omega_1,\omega_2) = \varphi_h(\omega_1) + \varphi_h(\omega_2) - \varphi_h(\omega_1+\omega_2), \tag{2.32}$$

where $\psi_y(\omega_1,\omega_2) = \angle S_{3,y}(\omega_1,\omega_2)$ and $\varphi_h(\omega) = \angle H(\omega)$. Clearly any linear phase component is canceled out whereas any other component of $\varphi_x(\omega)$ may be retrieved from the Bispectrum phase [Matsuoka and Ulrych, 1984] [Bartelt et al., 1984], [Kang et al., 1991], [Petropulu and Nikias, 1993] and [Dianat and Raghuveer, 1990].

It is interesting to notice the similitude of Eq. (2.30) with the one given for deterministic signals in section 2.1.6, Eq. (2.22). Actually the same conclusions about the phase of the

Power Spectrum and Bispectrum can be drawn and any method that retrieves the transfer function from the Bispectrum of the output sequence may be used to retrieve a deterministic signal from its Bispectrum. The same argument will be used in next chapter, where methods to estimate an MA system will be used to retrieve a deterministic signal.

2.1.8 Higher-Order Cepstra

The last definition of this survey introduces the concept of cepstrum. This transformation has several applications to nonminimum phase signal reconstruction and deconvolution. See, for example Oppenheim and Shaffer [1989, chapter 12] for definitions and Nikias and Petropulu [1993, Chapter 5] for extensions to the HOS domain. The *n*th-Order complex cepstrum of a discrete *n*th-order stationary random signal, $x(t)$, is defined as :

$$c_x(m_1,m_2,...,m_{n-1}) = F^{-1}\{ ln[S_{n,x}(\omega_1,\omega_2...,\omega_{n-1})]\} \tag{2.33}$$

where F^{-1} denotes the inverse Fourier transform operation, *ln* denotes complex logarithm. The existence of the *n*th-order complex cepstrum is discussed in [Tekalp, 1989] and [Dudgeon,1975].

In the third-order domain the Bicepstrum is defined as

$$c_x(m_1,m_2) = F^{-1}\{ ln[B_x(\omega_1,\omega_2)]\} \tag{2.34}$$

If $B_x(\omega_1,\omega_2)$ corresponds to the bispectrum of a deterministic signal (2.19), or the output of a stable LTI system driven by a third-order white random signal (2.25), it can be shown that the cepstrum is different from zero on the straight lines, $m_1=0$, $m_2=0$, $m_1=m_2$ [Tekalp, 1989], [Petropulu, 1994]. The non-zero coefficients define the cepstral coefficients which are related to the minimum and maximum phase components of the system (or deterministic signal). It can also be shown, [Petropulu, 1994], that the difference of the cepstral coefficients contain phase information while their sums contain magnitude information.

Another function of interest is the bicoherence index or normalized bispectrum of a sequence $x(t)$ which is defined as:

$$b_x(w1,w2) \triangleq \frac{B_x(\omega_1,\omega_2)}{\sqrt{P_x(w_1)P_x(w_2)P_x(w_1+w_2)}} \tag{2.35}$$

The complex cepstrum of the bicoherence, c_{bx} , is defined as the inverse Fourier transform of the complex logarithm of the bicoherence index: i.e..,

$$c_{bx}(m_1,m_2) = F^{-1}\{ ln[b_x(w1,w2)]\} \tag{2.36}$$

Rewriting (2.35) as:

$$b_x(w1,w2) = \frac{B_x(\omega_1,\omega_2)}{|B_x(\omega_1,\omega_2)|} = exp(j\psi_x(\omega_1,\omega_2)) \tag{2.37}$$

we get from (2.36):

$$c_{bx}(m_1,m_2) = j\,F^{-1}\{\,\psi_x(\omega_1,\omega_2)\} \tag{2.38}$$

That is, the cepstrum of the bicoherence index is the inverse Fourier Transform of the phase of the bispectrum.

We see from these definitions that higher-order cepstra may play an important role in phase reconstruction problems.

2.2 HOS in Image Processing

Image Restoration

The problem of image restoration refers to finding an estimate of the ideal image from its blurred and possibly noisy rendition. Often, noise can be characterized by a colored Gaussian process of unknown covariance. Some research works in this field exploit the fact that the Bispectrum of Gaussian processes are identically zero. Thus, Sadler [1989] considers the Bispectrum to estimate a randomly translating and rotating object from a sequence of noisy images . The work by Dianat and Raghuveer [1990] discusses the reconstruction of the phase of the Fourier Transform and its magnitude from the Bispectrum, they develop techniques to reconstruct images degraded by a jittery channel with additive tone interference. These works have succeeded in restoring images, however blur was not taken into consideration. Erdem and Tekalp [1990] address the problem of Blur identification. Their method is based on the detection of zero-crossing in the Bispectrum assuming that the signal does not have any zeros in this domain. In practice, this assumption is rarely met. Moreover it is usually the case for moderate blurs, (out-of-focus blurs and long term atmospheric turbulences), that the FT of the blur filter is real and strictly positive, therefore all zeros in the Bispectrum domain correspond to the signal. In addition, the phase of the Bispectrum corresponds exclusively to the signal. Based on this considerations, Petropulu and Nikias [1993] developed a technique, called BIRA, based on bicepstrum coefficients to reconstruct images degraded by 1D channels. In [Sayrol et al., 1993b] we utilized this method to restore images from their projections when 2D blurring filters degraded the image. However, the BIRA algorithm could not be applied to those projections which had Z-Transform with zeros on the unit circle. The Weight-Slice Algorithm (WS) [Fonollosa and Vidal, 1993], on the other hand, could recover the signal of

interest even if its Z-Transform has zeros on the unit circle. Although possible, the extension of the WS algorithm to 2-D would increase enormously its analytical complexity. In chapter 3, we present two algorithms that use the WS method over the 1-D projections of the image . Finally, these algorithms can also be applied to space imagery [Sayrol et al., 1993c]. In fact, one of the early applications of digital image restoration was to employ triple correlations to reconstruct astronomical images from short-exposure photographs [Hofmann and Weigelt, 1983], [Lohmann et al. , 1983] and [Lohmann at al., 1984].

Feature extraction

Another important application of HOS in a 2-D context is introduced by Chandran and Elgar [1992], [1993] where invariant Higher-Order Spectra features of projections are used for object classification. Higher-order spectra are translation invariant because translation produces linear phase shifts which cancel. A useful function of the Bispectrum is defined integrating the bispectral values along straight lines which pass through the origin in the bifrequency plane. It is shown that from these functions, invariants to translation, amplification or DC-level and scaling changes are derived. This is possible provided that the signal of interest is bandlimited and scaling does not introduce any aliasing. Finally rotation invariance is also achieved deriving invariants from the Radon Transform of the image and using the cyclic-shift invariance property of the discrete Fourier transform magnitude. Results on synthetic and actual images show isolated, compact clusters in feature space and high classification accuracy. This application was also treated by Giannakis and Tsatsanis [1990].

Texture analysis and synthesis

In the area of texture analysis and synthesis, important works have been done by Tugnait [1993] [1994], Zou and Giannakis [1992], [1994] and Hall and Giannakis [1993]. Statistical approaches to texture processing have largely relied upon random models which characterize the 2-D process in terms of its first- and second-order statistics, and therefore cannot completely capture phase properties of random fields which are non-Gaussian and /or asymmetric. In [Tugnait, 1993] and [Tugnait, 1994] 2-D noncausal autoregressive models, with possibly asymmetric support for synthesis of images are investigated. The gray level at an image pixel is characterized as a linear combination of gray levels at nearby locations in all directions and an additive non-Gaussian, higher-order white noise variable. In [Zou and Giannakis, 1992] and [Zou and Giannakis, 1994] nonlinear matching techniques that improve over linear equation methods in estimating parameters of non-Gaussian random fields are derived. It is shown there, that formulation of seasonal 1-D sequences (which are obtained by concatenation of the rows or columns of a 2-D field into a 1-D sequence), allow treatment

of semi-stationary 2-D models. A 2-D signal is called semi-stationary if it is stationary in one of the two dimensions. These models are used to generate synthetic space variant textures. A basis expansion approach is also proposed using prolate spheroidal sequences for parsimonious nonstationary modeling. In [Hall and Giannakis, 1993], a consistent parameter estimator for non-minimum phase, asymmetric non-causal, 2-D ARMA models is obtained by minimizing a quadratic-error polyspectrum matching criterion. HOS are used to derive and implement 2-D Gaussianity, linearity and spatial reversibility tests which validate the modeling assumptions. To conclude, the results presented in these works indicate that HOS-based random field models are appropriate for texture modeling.

Motion estimation

In the area of motion estimation, most authors assume that no noise is present on image sequences and therefore no precautions are taken. Thus, when the images are degraded most existing methods do not work properly and more robust techniques are necessary. On the other hand, noise can be realistically described as a colored Gaussian process. In such circumstances, Higher-Order Statistics may offer some advantages since cumulants of Gaussian processes are asymptotically zero. Two authors have begun to utilize HOS for motion estimation. Kleihorst et al. [1993] obtain the displacement by maximizing a third-order statistics criterion. However, it is assumed that image regions are non-symmetrically distributed when employing third-order statistics. Anderson & Giannakis [1991], [1994] also use HOS to estimate the displacement between two images. They have developed several algorithms based on a parametric cumulant method, a cumulant matching method and a mean kurtosis error criterion. We have found that this method works well for large size regions. Otherwise it is not clear the advantage over second-order statistics. The method we develop on the fourth chapter of this thesis is also based on a kurtosis measure, however, as we will see, the estimation allows smaller size regions [Sayrol, 1994].

2.3 General Framework

Usually, the problems of image sequence restoration and motion estimation, although different, can be analyzed using a generalized linear shift-invariant model formulated as,

$$g_k(m) = f_k(m) * h_k(m) + n_k(m), \tag{2.37}$$

where $m = (m,n)$ denotes the spatial image position of a point, $g_k(m)$ is the observed image intensity at time k, $f_k(m)$ is the noise-free image, $h_k(m)$ is a linear shift-invariant blurring point spread function (PSF) and $n_k(m)$ is additive noise.

Motion is not observable and cannot be directly measured. Therefore, it is imperative that a relationship between motion and image sequence be established. This relationship expresses assumptions about the properties of objects undergoing motion. Complex descriptors such as size, shape or structure of an object can be used, however, their evaluation is a difficult task. Alternatively, simple characteristics such as brightness, color or their derivatives can be employed, even tough they are insufficiently stable over long intervals. Assuming that time intervals are relatively short, the hypothesis that image brightness along motion trajectories is constant holds:

$$f_k(m) = f_l(c_l(m,k)) \tag{2.38}$$

where the function $c_l(m,k)$ describes the 2-D trajectory of an image point, i.e., $c_l(m,k)$ is the spatial position at time l of an image point that at time k is located at m. When $l=k-1$ and denoting by $d_k^o(m)$ the displacement of a point from time $k-1$ to k, Eq. (2.38) simplifies to

$$f_k(m) = f_{k-1}(m-d_k^o(m)) \tag{2.39}$$

Therefore Eq. (2.36) becomes

$$g_k(m) = f_{k-1}(m-d_k^o(m)) * h_k(m) + n_k(m), \tag{2.40}$$

When dealing with image restoration problems we are interested in obtaining $f(m)$ from the observation $g(m)$. In this case we assume $d_k^o(m) = d_k^o$, the trajectories are displacements which are the same for the set of all pixels in the image.

$$g_k(m) = f_{k-1}(m-d_k^o) * h_k(m) + n_k(m), \tag{2.41}$$

On the other hand, in image motion estimation we are interested in estimating $d_k^o(m)$ from $g_k(m)$ given at several time lags. In this case, the model is usually simplified to the case of no blurring, i.e., $h_k(m) = \delta_k(m)$ since, if it is unknown, the use of incorrect filters can do more harm than good. Thus, the equation that characterizes motion estimation problems can be described as :

$$g_k(m) = f_{k-1}(m-d_k^o(m)) + n_k(m), \tag{2.42}$$

At this point, the basic tools of HOS have been introduced from a signal processing perspective and a survey of HOS applications to image processing has been carried out. To conclude, a general framework that involves the two topics treated in this thesis has been established. In the following chapters, we thoroughly study these two problems, starting with the problem of Image Restoration.

CHAPTER 3

IMAGE RESTORATION USING HIGHER-ORDER STATISTICS

The use of higher-order statistics (HOS)-based methods is proposed to address the problem of image restoration. First, images degraded by linear or zero phase blurring point spread functions (PSF) and additive Gaussian noise are considered. A second degradation model for astronomical images is examined where the blur is caused by turbulent atmosphere and telescope aberrations. The restoration strategy in both cases is based on the fact that the phase information of the original image and its HOS, are not distorted by the blurring function. The difficulties associated with the combination of truly two-dimensional signals and their higher-order statistics are reduced by means of the Radon Transform. The projection at each angle of a 2-D image is an 1-D signal which can be processed by an 1-D higher-order statistics-based method. Methods that apply the Bicepstrum Iterative Reconstruction Algorithm (BIRA) [Petropulu, 1993] and the Weight-Slice Algorithm (WS) [Vidal, 1993] are developed. After the original projections have been estimated, the Inverse Radon Transform is employed to obtain the restored image.

In Section 1, the assumptions for the image observation model are described, including the blur and noise models. The projection theorem that yields to the processing of images from their projections is reviewed and, the BIRA and the WS method are also revisited. In Section 2, the theoretical bases that allow the reconstruction from either the phase of the Fourier Transform or the phase of the Bispectrum are established. In Section 4 three image restoration algorithms are developed. Some examples are given in Section 6. Finally, Section 7 is devoted to conclusions and final remarks.

3.1 Preliminaries

Every visual scene is an image that originates from a great variety of image formation processes that, fortunately, can be approximately described with a relative small number of equivalent physical concepts and an associated set of equations. Describing the processes and equations of image formation is motivated by the desire to provide image restoration. The techniques that deal with such problem are oriented towards modeling the degradations, blur and noise, and applying an inverse procedure to obtain an approximation of the original scene. The restoration concept is different from the enhancement concept which goal is to manipulate an image producing more visually pleasing results to an observer. Usually enhancement techniques do not consider degradation models.

The problem of image restoration has been extensively treated in the literature given its practical importance as well as its theoretical interest. Hence, an overview of such methods would be too extensive and laborious since the problem arises in almost every branch of engineering and applied physics. A state of the art in recent developments as well as a detailed introduction is presented in [Katsaggelos, 1991]. Another classical introductory book on this problem is [Andrews, 1977]. Additionally, a survey on digital image restoration is also given in [Sezan, 1990].

Perhaps one of the most prominent examples of successful image restoration was the work done at the Jet Propulsion Laboratory with images of the Moon, Mars and other planets from TV cameras on board of satellites [Huang, 1979]. A lot of research has been also carried out by imaging planets and stars through the atmosphere from systems based on earth. Atmosphere turbulence is also a severe limitation in remote sensing and aerial imaging used for geographic purposes or weather prediction. Another particular example where restoration techniques could have been useful was to restore images obtained from the Hubble Telescope, which suffered form a spherical aberration of its primary mirror. Perhaps, if applicable, the use of HOS-based methods, which are known to be "expensive techniques", would have been cheaper than sending a space shuttle to repair the telescope.

A typical imaging system consist of an image formation system, a detector and a recorder. For example, an electro-optical system such as the television camera, contains a photoelectronic device which is scanned for transmission or recording of the image. In any stage of the system images are likely to be degraded. The success of any image restoration scheme relies on how good the mathematical model fits the real image degradation. Here, we are concerned with two types of degradation: deterministic or random spatial degradation (the blur) and; random pointwise degradation (the noise). We address the problem of recovering images

from degraded versions of it, assuming a linear imaging system with space invariant point spread function (PSF) and additive noise. Thus, the discrete image model was given in Eq. (2.41) and it is rewritten here as:

$$g(m) = \sum_{m'} h(m-m')\, f(m') + n(m)$$

$$= h(m) * f(m) + n_k(m) = a(m) + n(m) \qquad (3.1)$$

where the time sub index k has been dropped, and will be used only when required. The displacement or shift d_k^o, has also been withdrawn since it is assumed the same for all pixels. Recall that $g(m)$ is the observed image intensity for the spatial position $m = (m,n)$, $f(m)$ is the noise-free image considered deterministic, $h(m)$ is a linear shift-invariant blurring point spread function (PSF) that can be either deterministic or random, $n(m)$ is symmetrically distributed random noise, m' belongs to the region of support of $h(m)$, and $a(m)$ denotes the 2-D convolution of $h(m)$ and $f(m)$.

The restoration objective is to obtain a signal as close as possible to the original image, $f(m)$, given $g(m)$, and having some knowledge of $h(m)$ and $n(m)$. Most restoration techniques based on statistical models make use of second-order statistics, ignoring the phase information. On the other hand, in many cases noise can be modeled as having Gaussian statistics of unknown covariance. Both facts combined, make HOS a potential tool to restore degraded images. A detailed motivation and development will be given throughout this chapter. Let us first obtain the bispectrum of an image that may be derived from the definitions provided in the previous chapter. The bispectrum of $g(m)$ is given by:

$$S_{3,g}(\omega_{11},\omega_{12};\omega_{21},\omega_{22}) = G(\omega_{11},\omega_{12})\, G(\omega_{21},\omega_{22})\, G(-\omega_{11}-\omega_{21}, -\omega_{12}-\omega_{22}), \quad (3.2)$$

where $G(\omega_1,\omega_2)$ is the 2-D Fourier Transform of $g(m)$. In the above expression a deterministic formulation is supposed. A stochastic formulation could be easily derived by taking the expectation of the above equation, see Eq. (2.17). Both formulations have to be kept in mind since we are dealing with deterministic signals, the original image and the blurring filter, and stochastic signals, random blurring filters and the noise.

Note that the Bispectrum is a 4-D signal from which the original noise-free image must be retrieved. The Weight-Slice Method is a HOS-based method capable of obtaining the signal of interest from its Bispectrum. It requires the inversion of the third-order cumulant matrix, which needs, for an image of size NxN, the order of $O(NxN)^3 = O(N^6)$ operations. This tremendous amount of computations, even for moderate values of N, must be reduced by

either using a less computationally expensive approximation or by processing the image in the projection domain. In the latter case, considering N projections of length N, the aforementioned method will require $O(N)\ O(N)^3 = O(N^4)$ operations. This number of computations is substantially lower and, thus, this solution is the one we adopt for the restoration of images. In order to ensure that the properties of the blur and noise are kept in this new domain, the projection theorem is first introduced. Hence, the mathematical description will be given for the 1-D projections of the image.

3.1.1 The Projection Theorem

The difficulties associated with the combination of truly two-dimensional signals and their higher-order statistics can be reduced by means of the Radon Transform, also called projection operator. In Computer Tomography (CT) problems the projection space arises naturally because of the data gathering mechanics. This coordinate system plays an important role in many other applications unrelated to CT. For example, two dimensional linear shift invariant filters can be realized by a set of decoupled one-dimensional filters by working in the projection space. The 2-D signal recovery problem, that we treat in this thesis, can be uniquely decomposed into many 1-D signal reconstruction problems. Other applications where projections are useful are image segmentation, geometrical analysis of objects and image processing applications requiring transformation between polar and rectangular coordinates [Jain,1989].

The Radon Transform of a 2-D continuos function $f(x,y)$ denoted $f_\theta(s)$, is an analog operation defined as the line integral of $f(x,y)$ along a line inclined at an angle θ from the x-axis and at a distance s from the origin (Fig. 3.1) [Deans,1983]. Each point in the (s,θ) domain corresponds to a line in the spatial domain. Mathematically it is written as:

$$f_\theta(s)=\int \int_R f(x,y)\ \delta(x\sin\theta-y\cos\theta-s)\ dx\ dy \qquad (3.2)$$

where R is an area containing the object of interest. In practice, we deal with discrete signals and in this case $f(x,y)$ is an ideal low-pass version of $f(m,n)$.

A fundamental relationship, the Projection Theorem, relates the 1-D Fourier Transform of the projection $f_\theta(s)$[1], with the central slice, at angle θ, of the 2-D Fourier Transform of the object $F(\omega_1,\omega_2)$ [Deans, 1983], [Jain, 1989]. We obtain:

---

[1]the variable s will now be used for discrete signals.

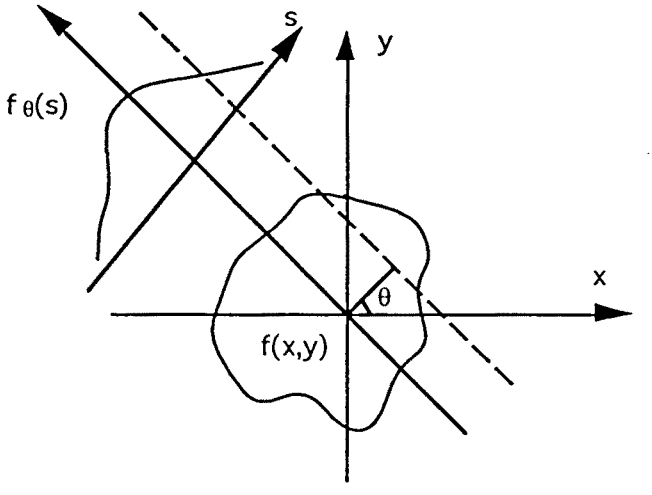

Fig. 3.1 Projection of $f(x,y)$ at angle θ

$$F_\theta(\xi)= \sum_{m=0}^{N-1}\sum_{n=0}^{N-1} f(m,n)\, e^{-j\xi(m\sin\theta-n\cos\theta)} \tag{3.3}$$

where $F_\theta(\xi)$ is the 2-D Fourier Transform in polar coordinates of $f(m,n)$ as well as the 1-D Fourier Transform of $f_\theta(s)$ with respect to s.

The example in Figure 3.2 shows that, taking sampled values for θ and ξ in the 2-D frequency domain, we end up with many more values at low frequencies than at high. The samples (full points) are spaced uniformly along the rays, but the distribution is not uniform in the ω_1-ω_2 Cartesian coordinate system. This implies that exact reconstruction of the original image from the discrete projections is not possible although very good approximations may be derived. Actually, much of the research in reconstruction algorithms deals with the proper compensation for the nonuniform distribution of the available values of the Fourier Transform [Tabei, 1992].

Despite this problem, restoration from projections is still feasible. As we will see in the examples, the problems inherent with implementing the Radon Transform are negligible as compared to the blur and noise degradations that deteriorate the image. See for example Fig. 3.11(a) and 3.11(b) and 3.12(a) and 3.12(b), where a couple of images are shown together with the same image after Radon and inverse Radon Transform.

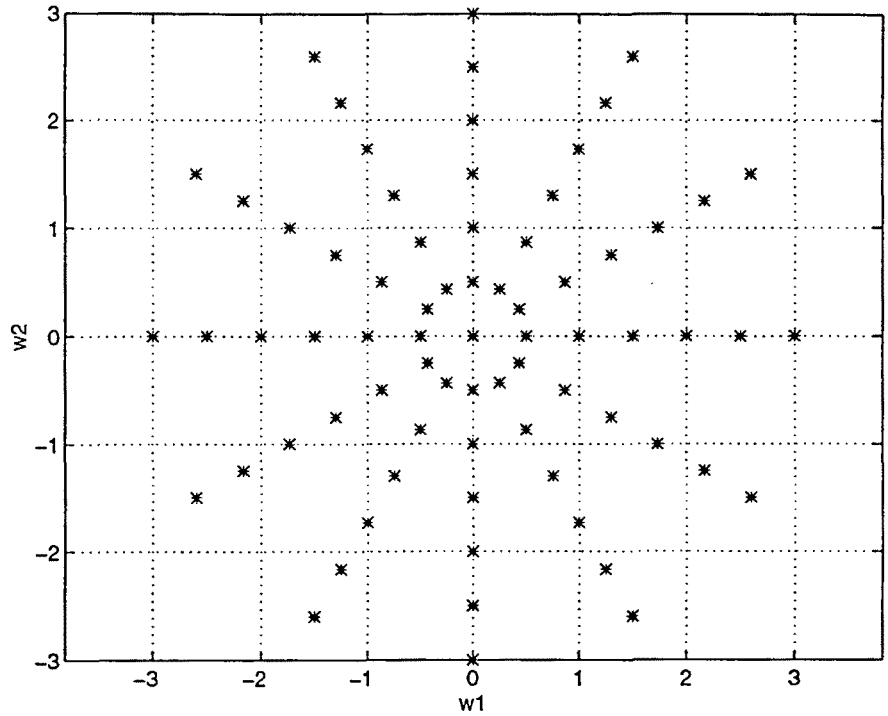

Fig. 3.2 Example of distribution of available values of the Fourier transform.

Let us now consider the projections of a blurred image. Denoting by $G_\theta(\xi)$, $A_\theta(\xi)$, $H_\theta(\xi)$ and $F_\theta(\xi)$ the Fourier Transforms in polar coordinates of $g(n,m)$, $a(n,m)$, $h(n,m)$, and $f(n,m)$ respectively, then, in the absence of noise:

$$G_\theta(\xi) = A_\theta(\xi) = H_\theta(\xi)\, F_\theta(\xi), \tag{3.4}$$

or taking Inverse Fourier Transform,

$$g_\theta(s) = a_\theta(s) = h_\theta(s) * f_\theta(s) \tag{3.5}$$

where $g_\theta(s)$, $a_\theta(s)$, $h_\theta(s)$, $f_\theta(s)$ happen to be the projections of $g(n,m)$, $a(n,m)$, $h(n,m)$, $f(n,m)$ at angle θ.

We can derive similar expressions for the projections of the Bispectrum. From the definition of deterministic Bispectrum and denoting by $B_{g\theta}(\xi_1,\xi_2)$ the Bispectra of $g_\theta(s)$, we obtain:

$$B_{g\theta}(\xi_1,\xi_2) = G_\theta(\xi_1)\; G_\theta(\xi_2)\; G_\theta(-\xi_1 - \xi_2).$$

From Eq. (3.4), in the noise-free case, the above expression becomes:

$$B_{g\theta}(\xi_1,\xi_2) = A_\theta(\xi_1)\, A_\theta(\xi_2)\, A_\theta(-\xi_1-\xi_2)$$

$$= H_\theta(\xi_1)\, F_\theta(\xi_1)\, H_\theta(\xi_2)\, F_\theta(\xi_2)\, H_\theta(-\xi_1-\xi_2)\, F_\theta(-\xi_1-\xi_2)\,.$$

Denoting by $B_{a\theta}(\xi_1,\xi_2)$, $B_{h\theta}(\xi_1,\xi_2)$ *and* $B_{f\theta}(\xi_1,\xi_2)$ the Bispectra of $a_\theta(s)$, $h_\theta(s)$ and $f_\theta(s)$, respectively, the last equation is equivalent to:

$$B_{g\theta}(\xi_1,\xi_2) = B_{a\theta}(\xi_1,\xi_2) = B_{h\theta}(\xi_1,\xi_2)\; B_{f\theta}(\xi_1,\xi_2). \tag{3.6}$$

Finally, denoting by $R_{g\theta}(s_1,s_2)$, $R_{a\theta}(s_1,s_2)$, $R_{h\theta}(s_1,s_2)$ and $R_{f\theta}(s_1,s_2)$ the triple correlations of $g_\theta(s)$, $a_\theta(s)$, $h_\theta(s)$ and $f_\theta(s)$, respectively, we can compute the Inverse Fourier Transform of Eq. (3.6) as:

$$R_{g\theta}(s_1,s_2) = R_{a\theta}(s_1,s_2) = R_{h\theta}(s_1,s_2) * R_{f\theta}(s_1,s_2) \tag{3.7}$$

Equations (3.6) and (3.7) imply that the convolution property that was valid for the image and for its projections can be extended to the third-order statistics of the projections.

3.1.2 Degradation Models

The formulation that deals with the projections of the image has been established taking into account the blur degradation only. Next, some considerations on the noise degradation are presented to later on retake the above expressions considering the presence of additive noise.

3.1.2.1 Noise in Imaging Systems

The noise process may originate in the image formation process, the transmission medium, the recording process or any combination of these. For example, in photographic film, the noise, called film-grain noise, is introduced by the silver grains that compose the developed image. The image is formed by the masses of silver deposited after development, but there is a fundamental randomness inherent in the grain deposition. The silver grains are randomly distributed with respect to their size, shape and location. Film-grain noise is signal-dependent and Poisson distributed which makes restoration algorithms particularly difficult [Huang,1968]. Fortunately, it can be approximated by a Gaussian process.

In photoelectronic systems the noise introduced is due, first, to the random fluctuations in the number of photons and photoelectrons on the active photoactive surface of the detector and, second, to the random thermal noise sources in the posterior circuits. The latter, has a behavior that is well-known, it is described as a zero-mean white Gaussian noise. The first

process generates signal-dependent noise governed by Bose-Einstein statistics [Andrews, 1977], which, for high light levels, is approximated by Gaussian statistics and it is considered independent of the signal.

A different type of noise that occurs in the coherent imaging of objects is called speckle noise. For low-resolution objects, it is multiplicative and occurs whenever the surface roughness of the object being imaged is of the order of the wavelength of the incident radiation. It is modeled as log-normal, where after using a logarithmic transformation, it is converted to a signal independent, additive process which is close to Gaussian when an integrating aperture is used [Wear, 1990].

As pointed out in [Sezan, 1990], almost all practical implementations of the restoration algorithms assume that observation noise is a zero-mean, white Gaussian process that is uncorrelated to the signal. Furthermore, it was suggested in [Walkup, 1974] that not much improvement can be obtained by modeling the noise as signal-dependent in the image estimation problems [Tekalp, 1991]. Thus, it is a good approximation to assume Gaussian noise independent of the signal in our degradation model although any other type of symmetrically distributed noise is allowed. Furthermore, the methods presented here can also deal with cases in which the Gaussian noise is colored.

Noise can be disregarded in many applications where the SNR is high and the degradation is not perceivable. Nevertheless, there are some situations where the signal power is low, this is, for example, the usual case in medical imaging. In such circumstances, restoration methods should have noise into account.

Our purpose is to recover each projection, $f_\theta(s)$, in non-ideal conditions. Next, we shall study two possible situations in which the reconstruction is possible. First, when the image is degraded by a deterministic PSF and additive Gaussian noise, and second, when the PSF is random of known statistics.

3.1.3.1 Deterministic Blur and Additive Noise Model

The first restoration problem we address involves deterministic PSF. We consider the Optical Transfer Function (OTF), which is the Fourier Transform of the PSF, to have linear or zero phase. This property of the 2-D blur is fortunately preserved in the projection domain. Thus, $H_\theta(\xi)$ is also linear or zero phase since it is just an slice of the 2-D filter in the frequency plane.

The blur model we assume is realistic since in many applications, blur degradations due to an important number of sources are considered to have linear or zero phase. For example, in [Sezan, 1991] models for real out-of-focus images are investigated. It is shown that the phase is either zero or linear.

A more general case of spatially invariant models will include the class of symmetric PSF where the OTF is obviously real but not strictly positive. In this case we could not easily separate the phase of the signal from the phase of the blurring. Only if we had $F_\theta(\xi)$ real and strictly positive, we could identify the phase of the blurring filter and therefore reconstruct the blurring filter prior to restoration. Nevertheless, this case is not much realistic since it depends on the nature of the image. Otherwise we need more information about the blurring PSF. Our goal is to show that it is possible and appropriate to restore blurred-noisy images once we have recovered the true phase of the Fourier Transform or the true phase of the Bispectrum.

Let $\varphi_{g\theta}(\xi)$, $\varphi_{a\theta}(\xi)$, and $\varphi_{f\theta}(\xi)$ be the phase functions of $G_\theta(\xi)$, $A_\theta(\xi)$, $F_\theta(\xi)$ respectively. Let us also denote by $\psi_{g\theta}(\xi_1,\xi_2)$, $\psi_{a\theta}(\xi_1,\xi_2)$ and $\psi_{f\theta}(\xi_1,\xi_2)$ the phase functions of $B_{g\theta}(\xi_1,\xi_2)$, $B_{a\theta}(\xi_1,\xi_2)$ and $B_{f\theta}(\xi_1,\xi_2)$. If the phase of the OTF is linear, the phase of the 1-D Fourier Transform of $A_\theta(\xi)$, differs from the phase of the Fourier Transform of the projection of the original image by a linear factor, therefore

$$\varphi_{a\theta}(\xi) = \tau_o\xi + \varphi_{f\theta}(\xi), \tag{3.8}$$

where τ_o characterizes the phase of the OTF. If τ_o is zero they are equivalent,

$$\varphi_{a\theta}(\xi) = \varphi_{f\theta}(\xi). \tag{3.9}$$

In the third-order domain,

$$\psi_{a\theta}(\xi_1,\xi_2) = \psi_{f\theta}(\xi_1,\xi_2), \tag{3.10}$$

where the linear phase component is canceled out.

In absence of noise $\varphi_{g\theta}(\xi) = \varphi_{a\theta}(\xi)$ and $\psi_{g\theta}(\xi_1,\xi_2) = \psi_{a\theta}(\xi_1,\xi_2)$. Then from $\varphi_{f\theta}(\xi)$ and $\psi_{f\theta}(\xi_1,\xi_2)$, $F_\theta(\xi)$ and $B_{f\theta}(\xi_1,\xi_2)$ are uniquely reconstructed except for a constant factor. The *uniqueness* of the reconstruction is explained in Section 3.2.

When the signal of interest is contaminated with noise, the original phase functions are no longer available. Nevertheless, we can estimate the Bispectra of the projections in the case many independent, although possibly shifted, observations of the image are available. Using the fact that the Gaussian processes have identically zero polyspectra of all order greater than

two, additive Gaussian noise may be rejected by computing the sample bispectrum of the observations of $g_\theta(s)$. Along with the phase retrievability property, see Eq. (2.32), this is one of the advantages of using the bispectrum as opposed to power spectrum. Our immediate goal is to obtain a good estimation of $B_{a\theta}(\xi_1,\xi_2)$ and therefore $\psi_{f\theta}(\xi_1,\xi_2)$ or $\varphi_{f\theta}(\xi)$. This estimation is computed from:

$$\hat{B}_{a\theta}(\xi_1,\xi_2) = \frac{1}{K}\sum_{k=1}^{K} G_{\theta k}(\xi_1)\, G_{\theta k}(\xi_2)\, G_{\theta k}^{*}(\xi_1+\xi_2) \tag{3.11}$$

where K is the number of observations. Estimates of the bispectrum of $a_\theta(s)$ are asymptotically unbiased at all frequency pairs if and only if the Fourier Transform of $a_\theta(s)$ at $\xi = 0$ is zero [Giannakis, 1989]. For a finite extent sequence, this means that the mean value of the signal should be zero. It was latter shown in [Sundaramoorthy, 1990] that, even if the signal has non zero mean, we can still obtain asymptotically unbiased estimates for all frequencies which do not lie in the axis $\xi_1 = 0$, $\xi_2 = 0$, and $\xi_1 + \xi_2 = 0$. We have extended these results in Appendix A and shown that when the relative shift among the projections has a uniform or triangular distribution, the Bispectrum estimation is only biased near the origin and limited to the axis $\xi_1 = 0$, $\xi_2 = 0$, and $\xi_1 + \xi_2 = 0$ when noise is white. Thus,

$$E\{\hat{B}_{a\theta}(\xi_1,\xi_2)\} = \begin{cases} B_{a\theta}(\xi_1,\xi_2) + A_\theta(\xi_1)\delta(\xi_1) + A_\theta(\xi_2)\delta(\xi_2) + A_\theta^{*}(\xi_1+\xi_2)\delta(\xi_1+\xi_2) & \xi_1\ \xi_2 \approx 0 \\ B_{a\theta}(\xi_1,\xi_2) & otherwise \end{cases}$$

(3.12)

We can take advantage of the fact that the phase of the Bispectrum is not biased at the origin since it is zero. However this is not true for the magnitude unless $A_\theta(0) = 0$, that is, when the signal is zero-mean. Then, regardless of the mean of $A_\theta(0)$, from the estimated bispectrum $\hat{B}_{a\theta}(\xi_1,\xi_2)$ we obtain $\hat{\psi}_{a\theta}(\xi_1,\xi_2)$ and therefore $\hat{\psi}_{f\theta}(\xi_1,\xi_2)$ from which, as we will see, we can reconstruct the signal of interest.

3.1.3.2 Random Blur Model : Turbulent atmosphere

Anyone who views an astronomical star with a large telescope will observe a blurred image consisting of a collection of small dots which are wiggling around. The resolution of conventional astrophotography with large telescopes is not limited by the diffraction on the finite aperture. The influence of the atmosphere is worse than aperture diffraction. The inhomogeneities of the atmosphere are in constant turbulent motion, with the results that instantaneous wavefront degradations fluctuate rapidly with time. To "freeze" the atmospheric degradations, thus eliminating any time averaging, it is necessary to use a short-exposure

time, from 0.1 to 0.001 second or less. The PSFs and OTFS encountered for short-exposure images are markedly different from their long-exposure counterparts. The PSF of a long-exposure image is a smooth and broad function, then the corresponding OTF is narrow and smooth. On the other hand, the PSF for a short-exposure image is a jagged and narrower function, whereas the corresponding OTF has significant fluctuations of both magnitude and phase. One of the most important facts about short-exposure images is that their quality is unaffected by the tilt component of the wavefront distortions. A tilt of the incident wavefront simply shifts the center of the image and affects the image in no other way. Provided the goal of the imaging experiment is to determine the structure of the object brightness distribution, but not its absolute position, tilt is of no consequence. On the other hand, for long-exposure images, changing tilt of the incident wavefront serves to broaden the PSF and narrow the OTF. Since the structure of the OTF is statistical in nature for the short-exposure case, the best we can hope to do in mathematically describing it is to calculate some of its average properties.

The short-exposure image of a point source is found to have a great deal of high-frequency structure, often referred as "speckle'. The average speckle size corresponds to that of the diffraction-limited Airy disk of the telescope [Goodman, 1985]. This gives the hope that short-exposure data will give diffraction-limited information about the object. If we were to gather a large set of short-exposure photographs and center them all in such a way as to remove the effects of pure image shift from frame to frame, a sum of these aligned images would yield an image that closely agrees with the predictions of a theoretical average short-exposure OTF [Goodman, 1885]. A. Labeyrie [1970] invented an alternative approach called Speckle interferometry, motivated by the observation that, whereas the ensemble average of the short-exposure OTF falls off comparatively rapidly, the ensemble average of the squared modulus of the OTF has significant value out to much higher frequencies. Latter, Lohmann at al. [1983], [1984] conceived a method based on triple correlations, considering the theories by Labeyrie, that was capable of reconstructing true diffraction-limited images. This method, called speckle masking, might be seen as a generalization of speckle holography, where the cross-correlation of speckle interferograms of the object with the corresponding speckle interferograms of a point source yields a true diffraction limited image of the object. The light from the reference point source and the object must pass through the same isoplanatic patch in order to form correlated speckle patterns. This condition limits the class of objects which can be studied with the holographic method. In speckle masking, multiplication of a speckle interferogram with the same but properly shifted interferogram forms a mask which can act as an artificial reference star.

We next provide the mathematical description of the speckle masking method (in 1-D since we process the projections of the image). Thus, a sequence of short exposure speckle interferograms, $i_k(x)$ is evaluated, each one given by :

$$i_k(x) = o(x) * p_k(x), \tag{3.13}$$

where $o(x)$ is the intensity distribution of the object and $p_k(x)$ is a random PSF, combination of the atmospheric turbulence and the telescope. For a space-invariant incoherent image forming system, the OTF is known to be :

$$P_k(\omega) = \int H(\omega') H(\omega' + \omega)\, d\omega', \tag{3.14}$$

where

$$H(\omega) = H_o(\omega)\, M(\omega). \tag{3.15}$$

$H_o(\omega)$ represents the pupil function of the telescope, for example, for a rectangular aperture, $P_k(\omega) = Tri(\omega/a)$, a triangular function that depends on the dimensions of the aperture. $M(\omega)$ represents the random turbulent atmosphere. The average energy spectrum of the image is related to that of the object by,

$$|\hat{I}(\omega)|^2 = |O(\omega)|^2\ |\hat{H}(\omega)|^2 \tag{3.16}$$

It is clear that the retrievable information about the object will in general not be complete, for it is the squared modulus of the object spectrum that is obtained, not the complex spectrum itself. In speckle masking the following quantity is evaluated,

$$\hat{R}_i(x_1,\sigma) = < [i_k(x_1) i_k(x_1-\sigma)] * i_k(x) > \Rightarrow R_o(x_1,\sigma) = [o(x_1) o(x_1-\sigma)] * o(x_1) \approx o(x_1) \tag{3.17}$$

where $< >$ indicates ensemble averaging and $\Rightarrow$ denotes compensation of the speckle masking transfer function [Lohmann, 1983]. σ is selected such that the product mask $[o(x_1)o(x_1-\sigma)]$ is approximately a δ function. In this case, cross correlation with the object yields to the object itself. The proper shift vector σ for a double star is identical to their separation, for other objects σ may be difficult to find. Generalization of σ in Eq. (3.17) by a variable vector x_2 is nothing else than the triple correlation,

$$\hat{R}_i\,(x_1,x_2) = R_o\,(x_1,x_2)\, \hat{R}_p\,(x_1,x_2) \tag{3.18}$$

which gives the Bispectrum in the frequency domain

$$\hat{B}_i(\omega_1,\omega_2) = B_o(\omega_1,\omega_2)\,\hat{B}_p(\omega_1,\omega_2). \tag{3.19}$$

The random medium $M(\omega)$ can be modeled as a stationary random process with independent zero-mean Gaussian real and imaginary parts, it is shown that the average Bispectrum of the transfer function, $\hat{B}_p(\omega_1,\omega_2)$, is strictly positive for all frequencies up to the diffraction limit [Lohmann, 1983]. Therefore :

$$\angle\,\hat{B}_i(\omega_1,\omega_2) = \angle\,B_o(\omega_1,\omega_2)\,. \tag{3.20}$$

The phase information of the Bispectrum of the object is given by the phase of the average Bispectrum of the observed intensities.

Several algorithms have been derived to retrieve the object from the average Bispectrum of the speckle interferograms. Usually, $\hat{B}_p(\omega_1,\omega_2)$ is obtained from accurate measurements of a point source, yielding to the object bispectrum by deconvolution. Other algorithms use speckle masking as it is given in Eq. (3.17). Both options present some drawbacks, the first one requires the measurement of an isolated star in the isoplanatic neighborhood of the object, whereas the second one requires the selection of a proper masking σ. As pointed out in [Dainty, 1989], it is desirable to use only the Bispectrum phase in the reconstruction. Therefore, as in the deterministic blur model, our purpose is to retrieve the object of interest from its true Bispectrum phase.

3.1.3 HOS-based methods

We consider HOS-based methods to restore images affected by one of the two blur models presented before. In the first model, deterministic blurring and additive noise, third-order statistics will reduce the presence of zero-mean symmetrically distributed noise while preserving the phase information. In the second model, the properties of the blur in HOS domains supply the true Bispectrum phase of the object. Before developing the restoration algorithms we briefly describe the Bicepstrum Iterative Reconstruction Algorithm (BIRA) [Petropulu, 1990] and the Weight-Slice (WS) Algorithm [Fonollosa, 1993], [Vidal, 1994] that yield to the desired signal from its third-order statistics.

3.1.3.1 BIRA

This method reconstructs a signal from the phase of its bispectrum. As mentioned in the previous chapter, higher-order cepstra are closely related to the phase functions. BIRA employs the cepstral coefficients, that for a signal $f_\theta(n)$ are defined as

$$A_{f\theta}(m) = \sum_{i=1}^{L_1} a_{i\theta}^{\,m} - \sum_{i=1}^{L_2} c_{i\theta}^{\,m} \tag{3.21}$$

$$B_{f\theta}(m) = \sum_{i=1}^{L_3} b_{i\theta}^{\,m} \tag{3.22}$$

where $a_{i\theta}, b_{i\theta}$, are the zeros inside and outside the unit circle respectively, and thus are related to the minimum and maximum phase components. The coefficients$c_{i\theta}$ are the poles inside the unit circle of the Z-transform of $f_\theta(n)$. Observe that for finite sequences $(L_2 = 0)$ this term is zero. The cepstral coefficients are related to the phase of the bispectrum as [Nikias, 1990]:

$$c_{bf\theta}(m,0) = -\frac{1}{m}\left(A_{f\theta}(m) - B_{f\theta}(m) \right), \qquad m > 0 \tag{3.23}$$

where $c_{bf\theta}$ was defined in Eq. (2.36). They are also related to the power cepstrum $c_{pf\theta}$, which is the cepstrum of the power spectrum:

$$c_{pf\theta}(m) = \begin{cases} -\frac{1}{m}[A_{f\theta}(m)+B_{f\theta}(m)] & m > 0 \\ \ln |A_{1f\theta}|^2 & m = 0 \\ -\frac{1}{m}[A_{f\theta}(-m)+B_{f\theta}(-m)] & m < 0 \end{cases} \tag{3.24}$$

where $A_{1f\theta}$ is a constant. The relationship with the signal itself is

$$f_\theta(n) = F^{-1}\{e^{F\{c_{f\theta}(m)\}}\}, \quad n=0,..,N-1 \tag{3.25}$$

where

$$c_{f\theta}(m) = \begin{cases} -\frac{1}{m} A_{f\theta}(m) & m > 0 \\ 0 & m = 0 \\ \frac{1}{m} B_{f\theta}(-m) & m < 0 \end{cases} \tag{3.26}$$

is the complex cepstrum of the signal.

Inspecting the above equations we observe that the desired signal may be obtained in the following way. Knowledge of the phase of the Bispectrum leads us to the difference of the

cepstra coefficients, Eq. (3.23). On the other hand, the power cepstrum gives the sum of the cepstra coefficients, Eq. (3.24). Thus both coefficient sequences $A_{f\theta}(m)$ and $B_{f\theta}(m)$ can be found and from Eq. (3.25) and Eq. (3.26) we compute the desired signal $f_\theta(n)$.

3.1.3.2 The WS Algorithm

As we have seen in the previous chapter, it is known that, for a causal and exponentially stable system which input is assumed to be an independent, identically distributed and non-Gaussian sequence, with skewness γ_{3x}, the output Bispectrum $B_y(\omega_1,\omega_2)$ exists and is given by

$$B_y(\omega_1,\omega_2) = \gamma_{3x} H(\omega_1) H(\omega_2) H^*(\omega_1 + \omega_2). \tag{3.27}$$

We can observe that finding the coefficients of the filter $H(\omega)$ in Eq. (3.27) is equivalent to estimating a signal from its bispectrum.

The Weight Slice (WS) Algorithm has been previously used to obtain the parameters of a possibly non-minimum MA system [Vidal, 1993]. The MA parameters can be expressed as a linear combination of cumulant slices. It was shown that if there is a set of weights that gives a causal slice, then the MA system can be identified. The system of equations is expressed as

$$S_c w = b_o \tag{3.28}$$

where S_c is the matrix of cumulants of order 2 or higher

$$S_c = \begin{bmatrix} C_{2x}(-q) & C_{3x}(-q,j) & C_{4x}(-q,j,k) & \dots \\ \vdots & \vdots & \vdots & \vdots \\ C_{2x}(0) & \vdots & \vdots & \vdots \\ \vdots & \vdots & \vdots & \vdots \\ C_{2x}(q) & \vdots & \vdots & \vdots \end{bmatrix} \tag{3.29}$$

Each matrix coefficient, C_{nx}, is the estimated n th-order cumulant of the output signal, w is the weight vector

$$w = (w_2,\ w_3(j),\ w_4(j,k),\ \dots)^t \tag{3.30}$$

and b_o is the coefficient vector:

$$b_o = (0 \dots 0\ 1 \dots b(q-1)\ b(q)) . \tag{3.31}$$

The unknowns are the vector w, and the last q elements of b_o

The matrix equation is solved in two steps :

1) Computation of the minimum norm weights that give a causal W-slice

$$S_u\, w_m = (0, \ldots, 0,1)^t,$$

$$w_m = S_u{}^{\#}\, 1, \tag{3.32}$$

where S_u is the matrix formed from the upper $q+1$ rows of S_c, and $S_u^{\#}$ denotes the pseudo inverse of S_u

2) Computation of the coefficients as

$$b_o = S_c\, w_m = S_c\, S_u{}^{\#}\, 1, \tag{3.33}$$

b_o is the estimated sequence we obtain using a combination of cumulants, thus:

$$f_\theta(n) = b_o$$

3.2 Uniqueness of the reconstruction from the phase functions

The restoration strategy for each projection is based on the fact that we have exact knowledge of its Fourier phase or its Bispectrum phase. Once we have this information we need to ensure that we can uniquely reconstruct the desired signal. We first show that it is possible to recover the sequence $F_\theta(\xi)$ from the phase of $A_\theta(\xi)$. Analogously, $B_{f\theta}(\xi_1,\xi_2)$ will be determined from the phase of $B_{a\theta}(\xi_1,\xi_2)$. Finally, $F_\theta(\xi)$ may be found from the phase of $B_{a\theta}(\xi_1,\xi_2)$.

Hayes [1980] and Oppenheim [1981] were the first to thoroughly study the importance of phase in signals. In general, the phase and magnitude of the Fourier Transform are independent functions, which implies that the signal can not be recovered from either of them alone. Nevertheless, for some cases, there is a certain relationship that can be exploited. For example when the signal is minimum phase or maximum phase, the log magnitude and phase are related though the Hilbert Transform [Oppenheim, 1989]. Hayes and Oppenheim realized that, under certain conditions, a discrete sequence is completely specified to within a scale factor by the phase of its Fourier Transform, without the restriction of minimum or maximum phase. The conditions under which this is possible were established in the following theorem [Hayes, 1980]:

Theorem 1 : *Let x[n] and y[n] be two finite sequences which are zero outside the interval* $0 \leq n \leq N-1$ *with Z-Transforms which have no zeros in reciprocal pairs or on the unit circle*[2]. *If* $\angle X(\omega) = \angle Y(\omega)$ *at N-1 distinct frequencies in the interval* $0 < \omega < \pi$, *then* $x[n] = \beta\, y[n]$ *for some positive constant* β.

We have derived an important consequence of this theorem:

Corollary 1 : *Let x[n] be a finite sequence which is zero outside the interval* $0 \leq n \leq N-1$ *and which number of zeros is* $N-1 = K_b-1 + 4P + 2P^*$, *where* (K_b-1) *is the number of non-reciprocal zeros, and P and P* are the number of reciprocal and real reciprocal pairs respectively. There is a unique sequence y[n], except for some positive constant factor, that is zero outside the interval* $0 \leq n \leq K_b-1$, *for which* $\angle X(\omega) = \angle Y(\omega)$ *at N-1 distinct frequencies in the interval* $0 < \omega < \pi$.

We have created a new set of conditions to reconstruct a sequence from another with the same Fourier-phase but different length. This is the case of projections blurred by a zero phase OTF. The reconstruction is only possible if the Z-Transform of *x[n]*, has the same zeros than the Z-Transform of *y[n]* plus necessarily the rest of zeros in reciprocal pairs. In our case these zeros will correspond to the zeros of the PSF. The proof of Corollary 1 follows from considering that it is false and leading to a contradiction of Theorem 1. To identify the sequence *y[n]* only K_b-1 points of its Fourier phase are needed. However our original signal *x[n]* is specified by *N-1* points of its Fourier phase. Therefore we need *N-1* points to ensure that all information about *y[n]* is contained in the Fourier phase of *x[n]*.

We are also interested in extending these results to 2-D sequences. This extension can be achieved by mapping the 2-D sequence into a 1-D sequence and then applying Theorem 1, although in this case, the election of the pairs of distinct frequencies (ω_1, ω_2) is not arbitrary (see Appendix B). Thus, we have stated a similar corollary for 2-D signals :

Corollary 2 : *if x[n,m] is a finite sequence of dimensions NxN then there is a unique sequence, y[n,m], except for some positive constant factor, with dimensions* $K_b x K_b < NxN$ *such that* $\angle X(\omega_1,\omega_2) = \angle Y(\omega_1,\omega_2)$ *at* $(N-1)^2$ *distinct frequencies in the region* $0 < \omega_1 < \pi$, $0 < \omega_2 < \pi$.

---

2 Although not demonstrated in [Hayes, 1980] the theorem could be modified to allow zeros on the unit circle.

Corollary 2 is a very important result since it demonstrates that a 2-D signal may be recovered from its 2-D phase function. In particular, the Bispectrum of a 1-D signal, which is a 2-D signal, may be recovered from its Bispectrum phase.

A related lemma was derived by [Petropulu, 1990], where it was shown that a signal may be uniquely reconstructed from its bispectral phase except for some positive constant and some integer shift:

Lemma 1 : *Let x[n] and y[n] be two finite sequences that satisfy the requirements of Theorem 1, and let* $\psi_x(\omega_1,\omega_2)$ *and* $\psi_y(\omega_1,\omega_2)$ *be the phases of the Bispectrum of x[n] and y[n] respectively. If* $\psi_x(\omega_1,\omega_2)=\psi_y(\omega_1,\omega_2)$ *at N(N-1)/2 discrete frequencies in the region described by* $0< \omega_1+\omega_2 \leq \pi$, $\omega_2 \leq \omega_1$, $\omega_1 \geq 0$, *then* $x(n) = \alpha y(n-n_0)$ *for some positive constant* α *and some integer* n_0.

As we did for Theorem 1 we can derived a corollary to allow reconstruction of a sequence from another with the same Bispectrum phase but different length.

Corollary 3 : *Let x[n] be a finite sequence that satisfies the requirements of Corollary 1. There is a unique sequence y[n], except for some positive constant factor and some integer shift, that is zero outside the interval* $0 \leq n \leq K_b-1$, *for which* $\psi_x(\omega_1,\omega_2)=\psi_y(\omega_1,\omega_2)$ *at N(N-1)/2 distinct frequencies in the region* $0< \omega_1+\omega_2 \leq \pi$, $\omega_2 \leq \omega_1$, $\omega_1 \geq 0$.

Corollary 3 is demonstrated from the demonstration of Lemma 1 and Corollary 1.

The restoration schemes that we have developed are based on the theoretical results stated in the Corollaries. Corollary 1 set the bases to reconstruct a 1-D signal degraded by a zero-phase OTF from the phase of the blurred signal. We can include the case of linear-phase OTF if it is previously compensated. The first WS-based algorithm we develop in this paper is based on this result. Corollary 2 set the theoretical bases to reconstruct the Bispectrum of a 1-D signal degraded by a zero-phase or linear OTF from its Bispectrum phase. This result is exploited in the second WS-based algorithm developed in this work. Finally, we have developed a BIRA-based algorithm exploiting Corollary 3.

3.3 Algorithms

3.3.1 Motivation

In the preceding sections we first revised the projection theorem and described an image model characterized by some type of noise and blur degradation. Later, the BIRA and Weight

Slice method were chosen as two possible methods to recover a sequence from the bispectrum or a combination of cumulants respectively. We then set the theoretical bases that allow the reconstruction of a 1-D signal or a 2-D signal from its phase functions. In this section, we derive different methodologies to solve the image restoration problem for the deterministic and random blur models.

We assume that a series of images is provided. For example, we might have several observations of the same image embedded in noise with possibly different phase shifts; or a sequence of images of an object moving in a noisy background; or a sequence of short exposure speckle interferograms, etc.

Given a set of shifted images we could solve the registration problem and do frame averaging which is optimal in the maximum likelihood sense. This would reduce the noise degradation however the shift for each of the images could be difficult and burdensome to find and we will still need to deblur the resulting image.

All the concepts we have previously seen in this chapter are of paramount importance and will now make sense in the reconstruction schemes. Thus, the structure of the algorithms is motivated by the following facts,

1) To avoid the high complexity associated with HOS of 2-D signals we restore images from their projections.

2) Use of HOS allows reducing the presence of Gaussian noise while retaining phase information from the signal.

3) Reconstruction from the phase information can be motivated considering the following properties and common assumptions: (i) The FT of a discrete finite length signal can be uniquely reconstructed from its phase (Corollary 1); (ii) analogously, the Bispectrum may be recovered from its phase (Corollary 2); (iii) a discrete finite length signal can be reconstructed from its Bispectral phase (Corollary 3); (iv) the phase from many blurring functions is zero or linear.

4) Finally, the WS method is chosen to retrieve the signal from its third-order moments since it is a robust and well-proven method. The BIRA method is also capable of reconstructing a signal form the phase of its Bispectrum

3.3.2 Restoration Scheme

Figure 3.3 shows the block diagram of the restoration process that summarizes the operations we effectuate for all algorithms.

In first place, for each degraded image $g_k(m)$, we compute the Radon Transform to obtain the projections for different angles. The Radon Transform is calculated from an interpolation of the Cartesian sampling grid to the Polar grid of the 2-D FFT of the image. There is an intrinsic loss of information in this operation. However using FFT lengths larger than the size of the image and using polynomial interpolations in each direction of order (m-1) for $m \geq 2$ [Press, 1990], we get good estimations for the projections. See [Tabei, 1992] and references therein for other implementations of the Radon Transform.

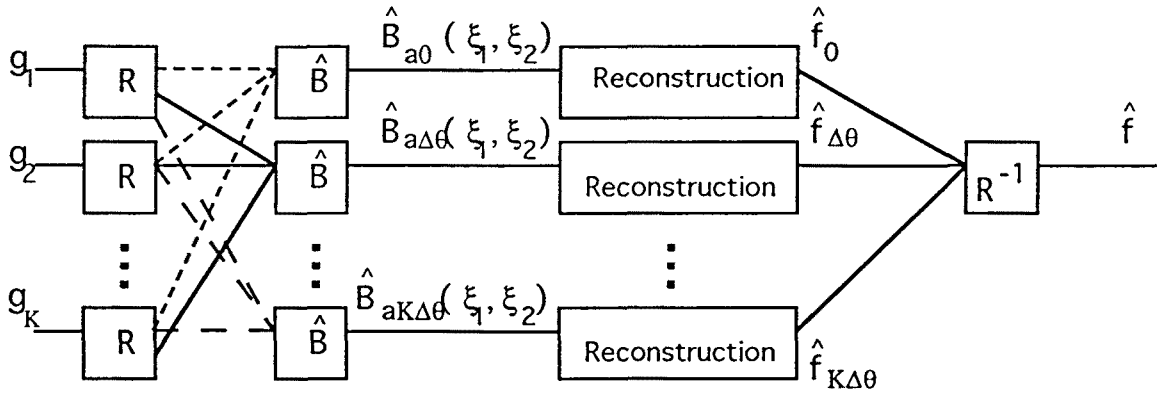

Fig. 3.3 Restoration scheme (R: Radon Transform; $\hat{B}$:Bispectrum estimation; R^{-1}: Inverse Radon Transform)

In the second step we calculate the third-order moment sequence or the triple correlation in the frequency domain for each projection and then, average over the realizations of the projections at the same angle [Nikias, 1993], as stated in Eq. (3.11). In the Bispectrum domain the presence of Gaussian noise is reduced.

In the following step we reconstruct the signal by using a HOS-based method. We have developed different methodologies based on the WS and the BIRA methods. In the next sections we will describe the reconstruction algorithms.

Finally, the Radon Inverse Transform gives the desired image. The Inverse Radon Transform is implemented reversing the Radon Transform procedure. That is, we interpolate from polar grid to Cartesian grid.

3.3.3 Algorithm 1: BIRA-based reconstruction

This algorithm has the main advantage to realize the reconstruction process in a single step: from the estimated bispectrum we reconstruct the deblurred signal (Fig. 3.4).

Fig. 3.4 Restoration scheme for the BIRA reconstruction

Such operation is implemented using an iterative algorithm that was developed in [Petropulu, 1993]. The algorithm starts from the true sequence of the phase of the bispectrum for at least $N(N-1)/2$ samples and an initial guess for the power cepstrum. It converges to a unique solution for the cepstral coefficients and consequently for the signal, except for a constant factor and a space shift. It is summarized in the following steps:

Step 1: Initialize the power cepstrum in Eq. (3.24) to an arbitrary value (one for all lags).

Step 2: Since the phase of the Bispectrum gives the differences of the cepstrum coefficients, estimate these coefficients from Eq. (3.24) and Eq. (3.23). Thus,

$$\hat{A}_{f\theta}(m) = \frac{-m\,\hat{c}_{pf\theta}(m) - 2mc_{bf\theta}(m,0)}{2} \qquad m>0$$

$$\hat{B}_{f\theta}(m) = \frac{-m\,\hat{c}_{pf\theta}(m) + 2mc_{bf\theta}(m,0)}{2} \qquad m>0 \qquad (3.34)$$

Step 3: Reconstruct $\hat{f}_{\theta}(n)$ from Eq. (3.25) and Eq. (3.26)

Step 4: Correct any linear phase component and set the length of the signal, multiplying $\hat{f}_{\theta}(n)$ by the following window:

$$R_{i\theta}(s) = \begin{cases} 0 & if\ (N-Int\ (K_b/2))-n_o \le n < L-n_o-1+Int\ (K_b/2) \\ 1 & otherwise \end{cases} \qquad (3.35)$$

Where L is the size of the FFT used in Eq. (3.25), n_o is the time shift that is introduced due to the reconstruction from the cepstra coefficients, K_b is the length of the blurring filter and $Int(x)$ indicates the closest integer smaller than x.

Step 5: Update the power cepstrum and go to Step 2 until the algorithm converges.

For further details on the algorithm see the aforementioned reference. We have changed Step 4 in order to restore blurred signals that obey the conditions settled in Corollary 3.

At this point we are really concerned in knowing if zeros of the Z-Transform of image projections lie on the unit circle. In this case the cepstral coefficients are infinite length sequences and may not be used. We studied projections of some well known test images : *"camman.pic"*; *"building.pic"*; *"face.pic"*; *"mandril.pic"*; *"hat.pic"*. Unfortunately, all projections had their zeros near the unit circle and most of them had some zeros on the same unit circle (considering four decimal precision). We took a window of size 60x60 from *"hat.pic"* and studied the projection at angle 0. This signal does not have any zero on the unit circle but all of them remain very close (the closest one has $| r | = 0.9996$).

Figure 3.5 shows the position of zeros for the Z-Transform of this projection.

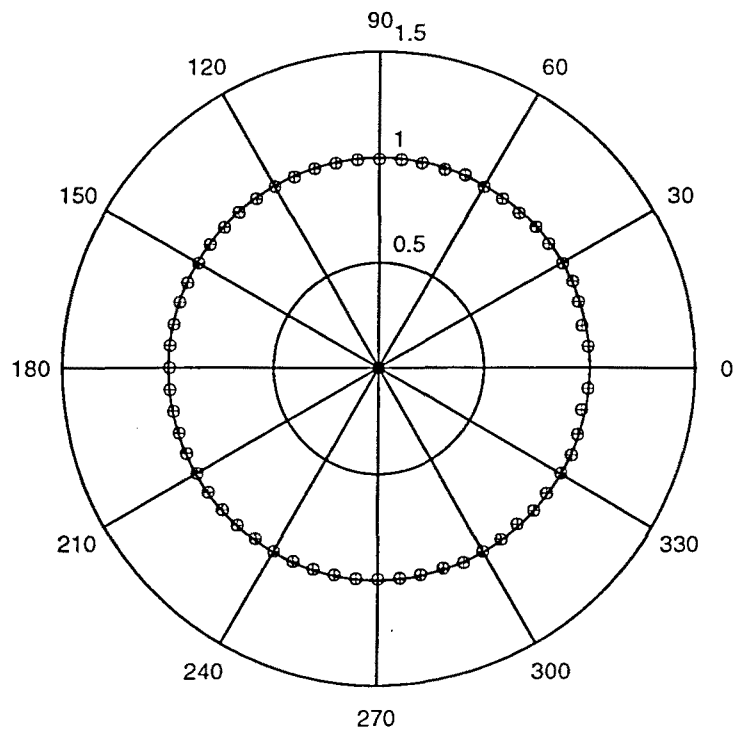

Fig. 3.5 Position of zeros for a projection at 0 degrees of a 60x60 window of "hat.pic"

We tested BIRA when no degradation was affecting this image. The cepstral coefficients were computed taking 2048 samples. The length of the FFTs was $L=10^{12}$. Figure 3.6 shows the reconstructed signal after 30 iterations. Although we have recovered the signal, the results are not worthy enough since no degradation was present and data lengths were too large. Moreover, the conditions were propitious since there were no zeros on the unit circle. Consequently we have discarded this method in our examples since, a priori, we do not know if a given image has its projections with zeros on the unit circle and, as we have seen for many test images, this unfortunate situation is very likely.

3.3.4 Algorithm 2: WS-Fourier Phase reconstruction

To avoid the problems associated with BIRA we look for an alternative HOS method which is capable of reconstructing a signal even if zeros are close to the unit circle. The Weight Slice Algorithm is one such method. However this algorithm realizes the reconstruction process in two steps : first, from the estimated bispectrum we reconstruct the projections by means of the WS itself (noise has been removed, however the signal is still blurred); second, we "deblur" this signal by Fourier phase reconstruction means. Figure 3.7 illustrates this procedure.

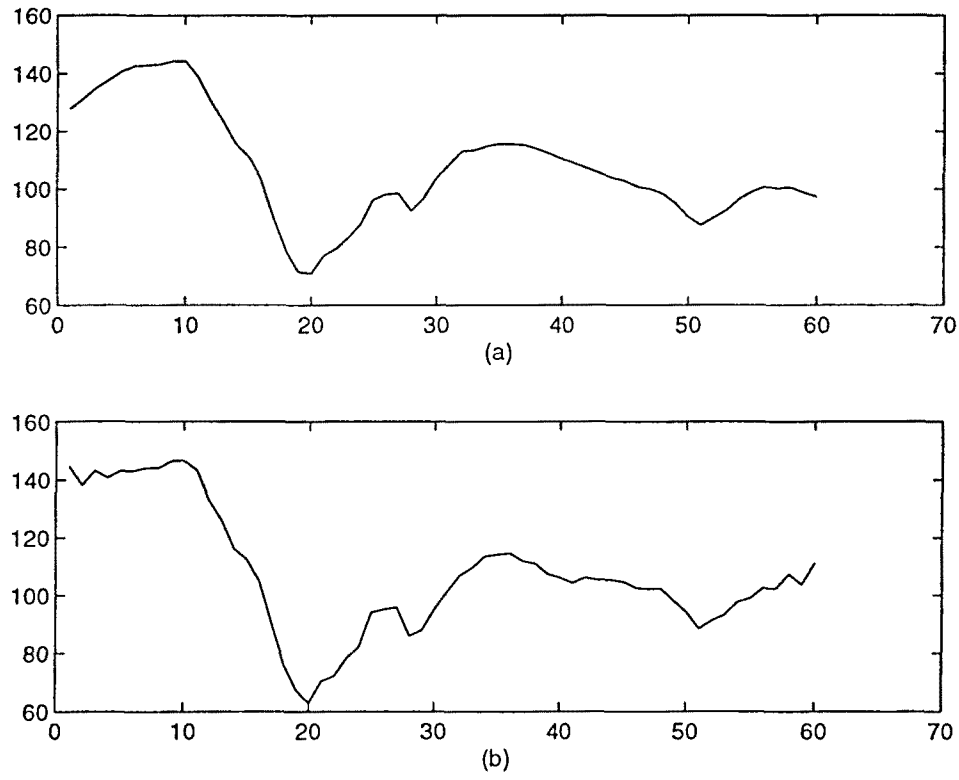

Fig. 3.6 a) projection at 0 degrees of "hat.pic". b) Reconstruction form cepstral coefficients using BIRA

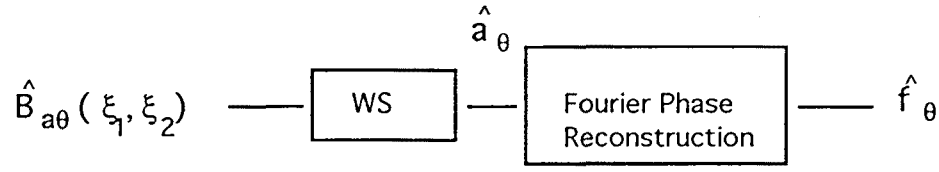

Fig. 3.7 Restoration scheme for the WS-FP reconstruction algorithm

In first place, we obtain the estimated sequence through the WS Algorithm. We only make use of the third-order moment sequence. Therefore $S_c = \hat{R}_{a\theta}(s_1,s_2)$, that is, the inverse 2-D FT of the estimated Bispectrum, of size *(2N-1, 2N-1)* . The matrixS_c is used in Eq. (3.32) to obtain the pseudoinverse and then the minimum norm weights. This result is used in Eq. (3.33) to find $b_o = \hat{a}_\theta(s)$ of length *N*.

In the next step, we obtain $\hat{f}_\theta(s)$ from the phase of $\hat{a}_\theta(s)$. We use an iterative algorithm similar to the one proposed in [Hayes, 1980]. Some modifications are necessary to adapt the scheme to the new set of conditions established in Corollary 1. The algorithm is the following:

Step1: Obtain the M-point DFT of $\hat{a}_\theta(s)$ and derive its phase function $\hat{\varphi}_{a\theta}(\xi)$ $\xi = 0, ..., M-1$ where $M \geq 2N$.

Step 2: Form another sequence $y_{i\theta}(s)$ given by

$$y_{i\theta}(s) = \begin{cases} 0 & 0 \leq n < Int\,(K_b/2) \\ \hat{f}_{i\theta}(s) & Int\,(K_b/2) \leq n < (N-Int\,(K_b/2)) \\ 0 & (N-Int\,(K_b/2)) \leq n \leq M-1 \end{cases} \qquad (3.36)$$

where $\hat{f}_{1\theta}(n) = \hat{a}_\theta(s)$.

Step 3 : Obtain a new estimation $\hat{F}_{i+1\theta}(\xi) = |Y_{i\theta}(\xi)| \exp(\hat{\varphi}_{a\theta}(\xi))$, where $Y_{i\theta}(\xi)$ is the M-point DFT of $y_{i\theta}(s)$ and $\hat{F}_{i+1\theta}(\xi)$ is the M-point DFT of the new estimated signal, $\hat{f}_{i\theta}(s)$.

In the first iteration of Step 2 we use the blurred signal. We set to zero the left and right margins to obtain a signal with the same length than the one we are trying to reconstruct. That

provides a convenient initial guess for the magnitude of the Fourier Transform and at the same time speeds up the process. Steps 2 and 3 are repeated until the algorithm converges.

It must be pointed out that any linear phase factor should be corrected before applying Step 2 in the reconstruction algorithm, otherwise the iterative procedure will not converge to the right solution. For the case of an object or an image in a noisy background a linear phase on the blurring filter causes a linear shift of the object and therefore to its projections. The linear shift is lost in the third order domain (this is why we can average many shifted projections in this domain). A simple mechanism that consist on choosing one position for the image been reconstructed is added. One of the image series is chosen and the shift is settled according to the shift of each projection of this particular image. For the case of complex shape objects we need more information to avoid shift errors among projections. For simple objects this information may be easily extracted, for example for binary stars two perpendicular projections are enough to locate the object.

3.3.5 Algorithm 3: Bispectrum Phase-WS reconstruction

The previous algorithm uses the estimated Bispectrum which magnitude is biased near the origin. If we were to use the phase of the Bispectrum we will avoid this problem. We suggest a third algorithm that reconstructs the true Bispectrum of the projection from the phase of the Bispectrum of the blurred signal. We then retrieve the signal using the WS method. Figure 3.8 illustrates this procedure, we observe that the two WS-based algorithms involve similar operations but in a reverse order.

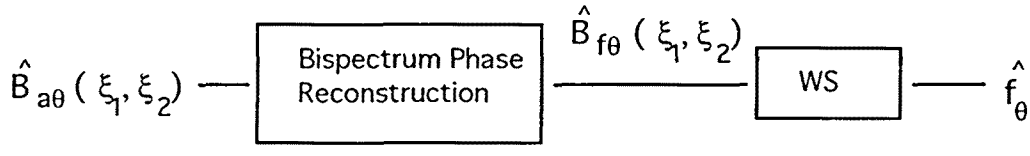

Fig. 3.8 Restoration scheme for the third algorithm

To retrieve the Bispectrum of the object from the 2-D Bispectrum phase of the interferograms we implement an analogous iterative algorithm to the one we presented for Algorithm 2. The new intervals in step 2 take into account the third-order moment region of support depicted in Fig. 3.9. For signals of length $N1$ the third-order moment sequence is zero outside an outer

hexagonal region [Mendel, 1991]. Suppose we know the dimensions of the object to be N_2, where $N_2 < N_1$, in this case the region of support is the inner hexagonal region (Fig. 3.9). Its boundaries establish the new intervals in the iterative algorithm. We could also speed up the process by taking advantage of the symmetry regions of third-order moments and use only the samples in the region $0 \leq n_1 \leq N_1, 0 \leq n_2 \leq N_2, n_1 \geq n_2$.

In the second step, the WS Algorithm reconstructs the signal from its moments. Hence $S = \hat{R}_{f\theta}(s_1,s_2)$ with size $(2N_2\text{-}1, 2N_2\text{-}1)$ and $b_0 = \hat{f}_{\theta}(s)$ of length N_2. Like for the previous algorithm, after this step, any linear phase factor should be corrected before projecting back the image.

Comparing the last two algorithm we observe that Algorithm 2 is faster since the iterative step is performed over 1-D sequences. However, the reconstruction uses the magnitude and phase of the estimated Bispectrum. On the other hand, in Algorithm 3 the reconstruction is only based on the phase of the estimated Bispectrum which is unbiased. Nevertheless the computational load of this algorithm is higher since the iterative procedure is applied to 2-D sequences.

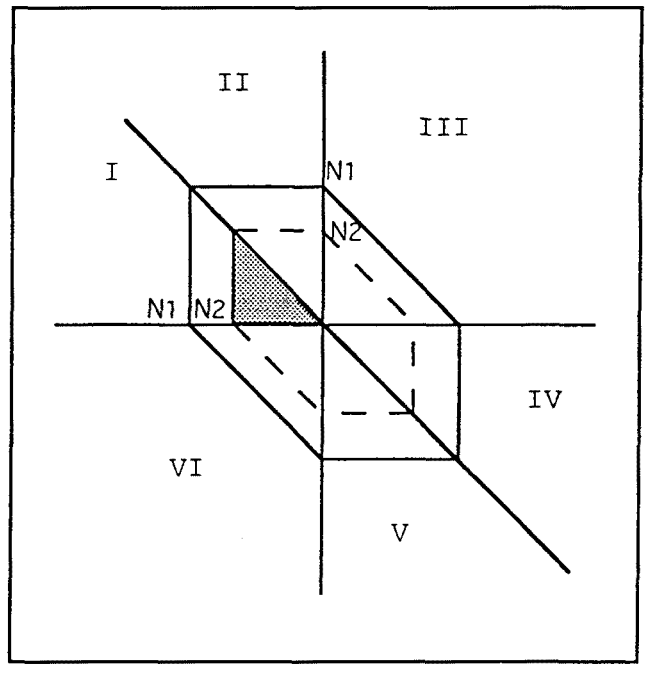

Fig. 3.9 Third-order moment region of support for sequences of length N_1 and N_2. The symmetry regions from I to VI are also shown.

3.3.5 Computational Complexity for the WS-based method

As it is well known, higher-order statistics methods are computationally more expensive than second-order ones. The computational burden arises from the sample mean estimation of moments or cumulants and of course from the corresponding reconstruction methods. Thus, the computational burden of the two WS-based algorithms to restore each projection is given by:

1) the sample estimation of the Bispectrum which is the same for all algorithms and of order $O(2KN^2)$, where K is the number of available realizations and N the length of the signal. In general, the order of operations is given by the number of lags, in this case N^2, the order statistics and the number of realizations.

2) the WS which requires $O(20/3\ N^3)$, [Vidal, 1993], operations for Algorithm 2 and $O(20/3\ (N-K_b)^3)$ for Algorithm 3. The computational complexity is due to the size of the cumulant matrix S_c since any algorithm solving pseudoinverse problems requires around m^3 for a matrix of size mxm

3) the iterative reconstruction procedure which differs for both algorithms. We see that for each iteration we basically compute an FFT and an inverse FFT. Thus, the second step in Algorithm 2 entails a computational cost to $O(2I_1 M log_2 M)$, where I_1 is the number of iterations and M the size of the FFT. For Algorithm 3, it requires $O(2I_2 M_2^2 log_2 M_2^2)$ operations, where $M_2 x M_2$ is the size of the 2D FFT and I_2 is the number of iterations

3.4 Results and comparisons with other methods

Example 1 : This example illustrates the performance of the iterative phase reconstruction step in Algorithm 2 for a typical projection. Fig. 3.10 (a) shows the original projection of an image that was blurred by a 3x3 Gaussian filter:

$$h(m,n) = exp(-\alpha(m^2+n^2)) \tag{3.37}$$

where α was set 0.7. The blurred projection is shown in Fig. 3.10 (b). We use FFT's of dimension 128 and 50 iterations to reconstruct the signal. Fig. 3.10 (c) is the reconstructed signal and Fig. 3.10 (d) the difference error signal. The reconstructed signal is very close to the original one, altough small errors show off in the error signal (notice the scaling is different).

Example 2 : This example demonstrates the performance of Algorithm 2 in the absence of noise for an arbitrary image. The original image is 64x64 and is shown in Fig. 3.11 (a). The 2-D FFTs to compute the projections are 256x128. Fig. 3.11 (b) is a blurred version of this image with a 5x5 Gaussian filter (α = 0.35). Fig. 3.11 (c) is the restored image from the Fourier phase. From this image we see that high frequencies have been properly recovered. However, we observe some distortion. This is due to relative small shifts among projections and to small errors in the reconstruction, like in the previous example. For low SNR these two sources of errors from projections will be stressed.

Example 3 : In this example we show the performance of the second algorithm and compare the restoration when other existing methods are applied. The original image is a computer generated image shown in Fig. 3.12(a). The reconstructed image after applying Radon Transform followed by the Inverse Radon Transform is shown on Fig. 3.12(b). The dimensions of the 2-D FFT and 2-D IFFT for the Radon Transform computation are 64x64 to avoid distortion in the high frequencies. Fig. 3.12(c) presents a blurred version of this image when a 3x3 Gaussian filter with α = 0.7 is utilized. Fig. 3.12(d) shows the restored image obtained from Algorithm 2. The phase reconstruction step is applied with FFT's of dimension 128 and 50 iterations. In Fig. 3.12(e) the image is blurred with the same filter and Gaussian noise for SNR[3]=25 dB is added. The restored image is shown in Fig. 3.12 (f) when Algorithm 2 is used. The third-order moments are estimated from 50 shifted realizations. To compare this result with a correlation-based method we consider in Fig. 3.12 (g) the parametric Wiener filter given by

$$\hat{F}(\omega_1,\omega_2) = \frac{H^*(\omega_1,\omega_2)}{|H(\omega_1,\omega_2)|^2 + \lambda \dfrac{P_{no}(\omega_1,\omega_2)}{P_f(\omega_1,\omega_2)}} G(\omega_1,\omega_2) \qquad (3.38)$$

where $P_{no}(\omega_1,\omega_2)$ *and* $P_f(\omega_1,\omega_2)$ are the periodogram-based estimates of the power spectra of the noise and the image, that are obtained considering 50 noisy realizations and $\lambda = 1$ [Andrews, 79]. A modified version of this filter is suggested in [Kang, 91], where the Fourier phase of the restored image is estimated from the Bispectrum. In Fig. 3.12 (h) we show the restored image from the magnitude of the parametric Wiener filter and the true phase of the signal. As we can observe, the method proposed in this paper gives better results than

---

[3]The signal-to-Noise Ratio for a 2-D signal f(n,m) of dimensions NxN is defined as $\dfrac{\sum_n \sum_m f^2(n,m)}{N^2 \sigma^2_n}$, where σ_n^2 is the variance of the noise.

the Wiener filter and similar results when the true phase is incorporated. However we must point out that the WS restoration scheme does not make use of the blurring filter, only its size. In this sense this method realizes a blind restoration.

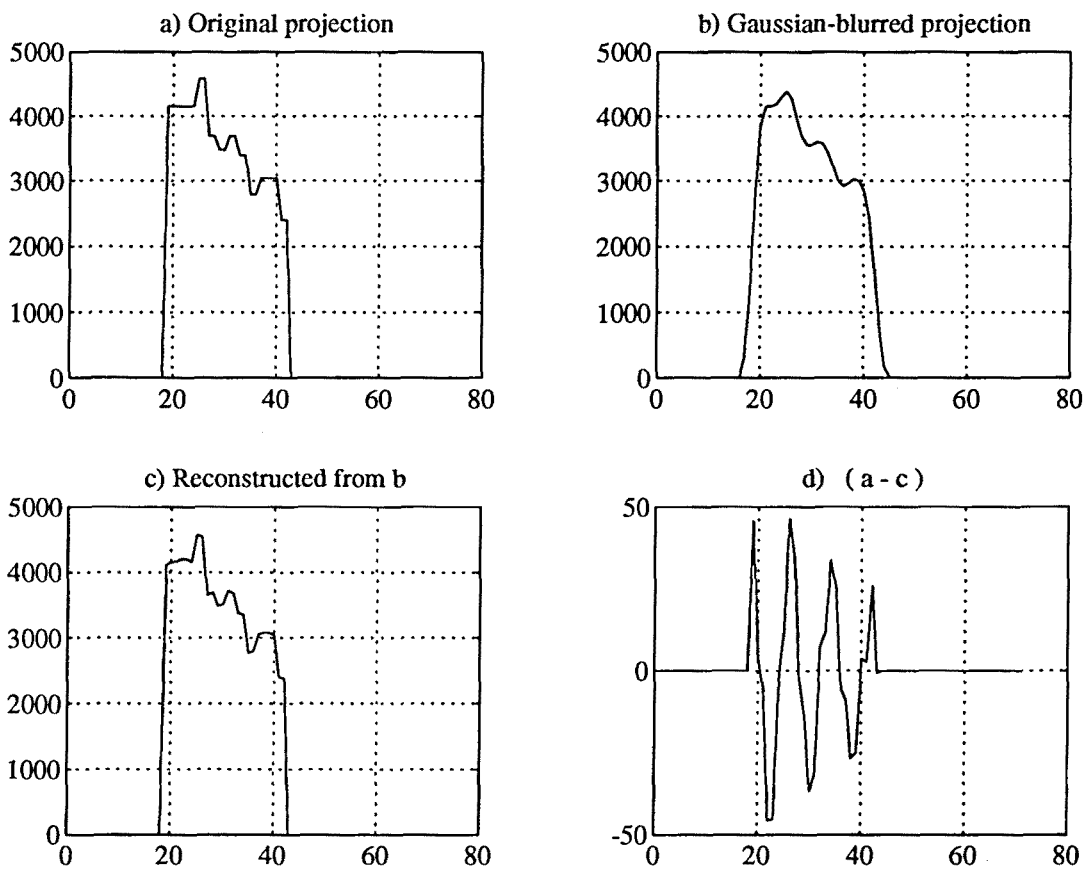

Fig. 3.10 Example of reconstruction from the phase of the FT using 128-point FFT and 50 iterations.

(a)

(c)

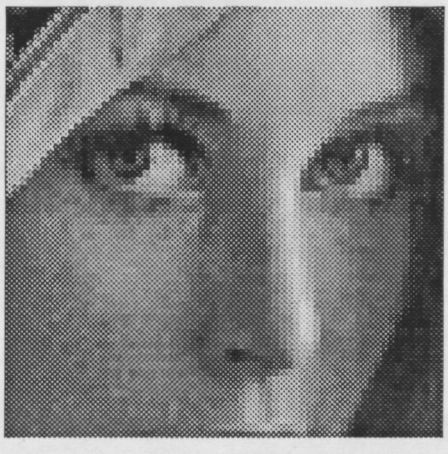

(b)

(d)

Fig. 3.11. (a) Original image. (b) Image obtained after applying Radon and Inverse Radon Transform. (c) Blurred Image by a 5x5 Gaussian filter, $\alpha = 0.35$. (d) Restored image from (c) using Algorithm 1.

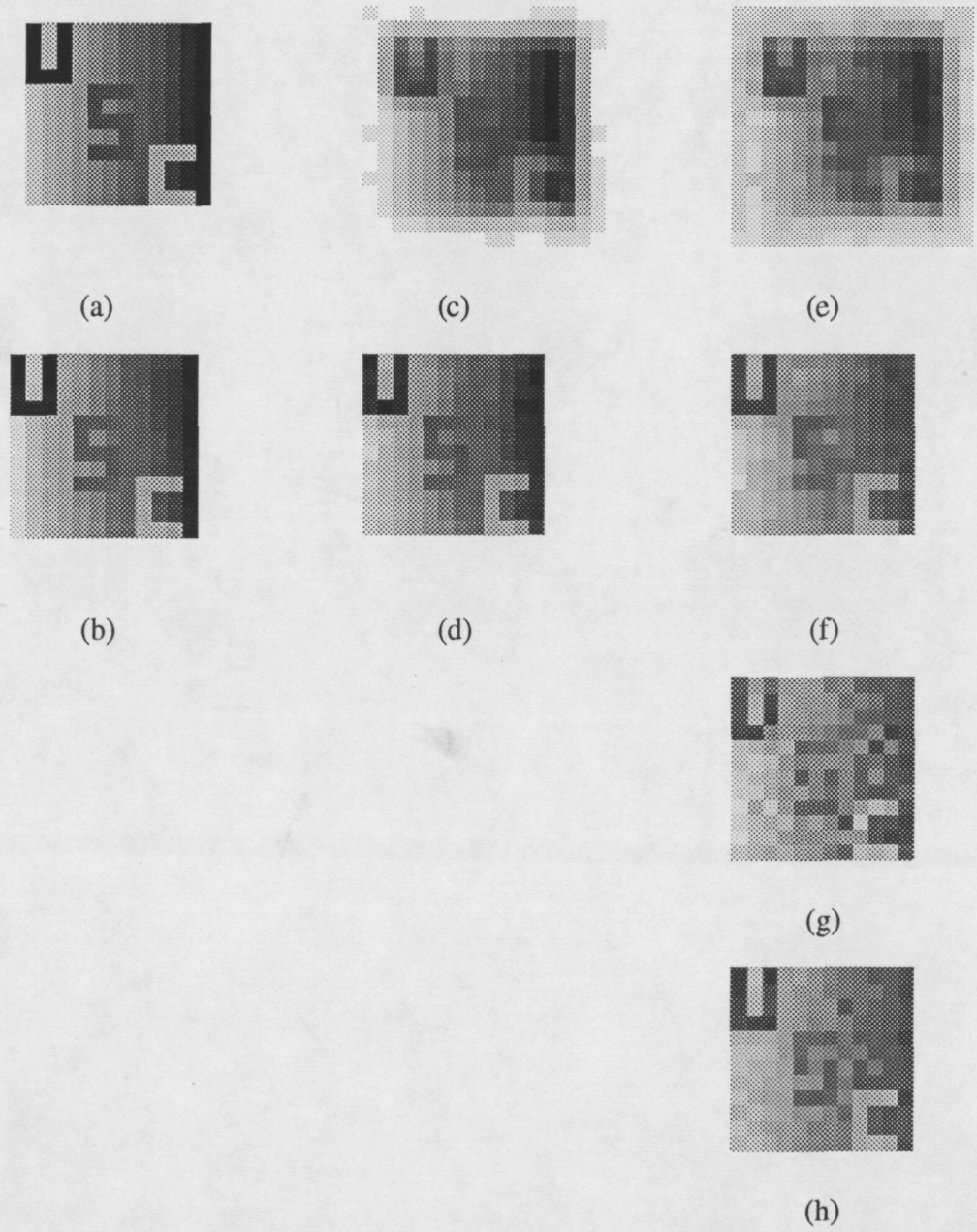

Fig. 3.12 (a) Original image. (b) Image obtained after applying Radon and Inverse Radon Transform. (c) Blurred Image by a 3x3 Gaussian filter, $\alpha = 0.7$. (d) Restored image from (c) using Algorithm 2. (e) Same as (c) but SNR = 25 dB. (f) Restored Image from (e) using Algorithm 2. (g) Restored image using Parametric Wiener Filter. (h) Restored image using Parametric Wiener Filter and the true phase of the signal.

Example 4 : In this experiment we compare the algorithms in a low SNR scenario. Figure 3.13 (a) corresponds to the projection of the image in Fig. 3.10 (a) at angle 0 degrees. Figure 3.13 (b) corresponds to the same projection when the image is degraded by a 5x5 Gaussian blurring filter with α=0.9 and the SNR=5 dB, 50 noisy and shifted realizations are available (the shift is randomly generated with uniform distribution between +8 and -8).

The results using the parametric Wiener filter and the modified Wiener filter are shown in Figs. 3.13 (c) and 3.13 (d). The small details have been lost and even if we use the true phase of the signal we can not properly restore the original projection. Figures 3.13 (e) and 3.13 (f) show the results using Algorithm 2 and Algorithm 3 respectively, where the FFT size and the number of iterations are 256 and 50 for the second algorithm and 256x256 and 25 for the third one. The restoration is better accomplished by Algorithm 3 (except at the extreme of the signal) at the expense of a higher computational cost. We have computed the error from $e = \Sigma (\hat{f}_0(s) - f_0(s))^2$ and obtained $e = 22.00\ 10^3$ for the parametric Wiener filter, $e = 21.70\ 10^3$ for the modified parametric Wiener filter, $e = 1.28\ 10^3$ for Algorithm 2 and $e = 1.08\ 10^3$ for Algorithm 3. We clearly see that high frequencies are better preserved and the error is much lower when the proposed algorithms are utilized. Unfortunately, as was mentioned before, for this low SNR, although the quality of the 1-D projection has been considerably improved, small error contributions from all projections will be propagated and added up to the final image. Thus the resulting final image was not satisfactory.

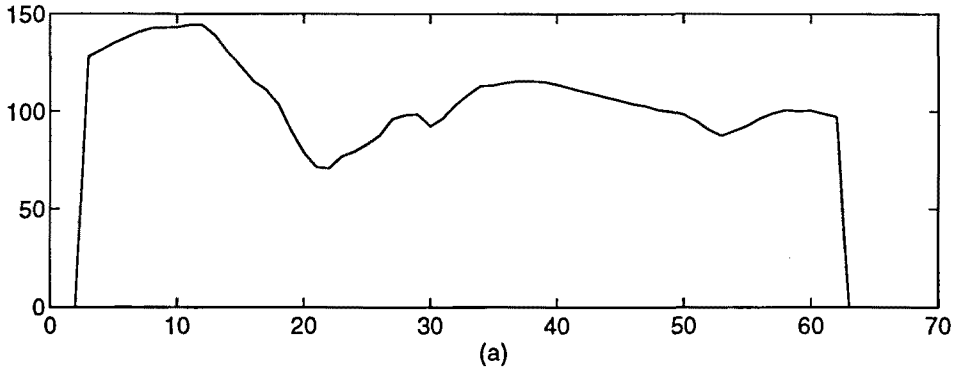
150
100
50
0
0
10
20
30
40
50
60
70
(a)

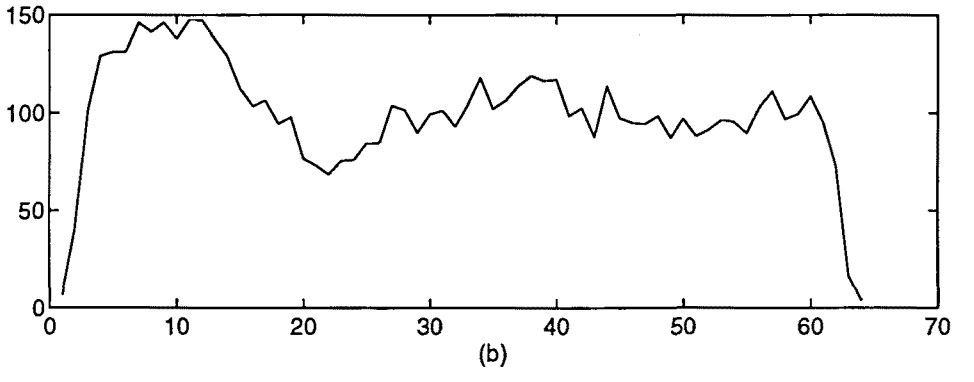
150
100
50
0
0
10
20
30
40
50
60
70
(b)

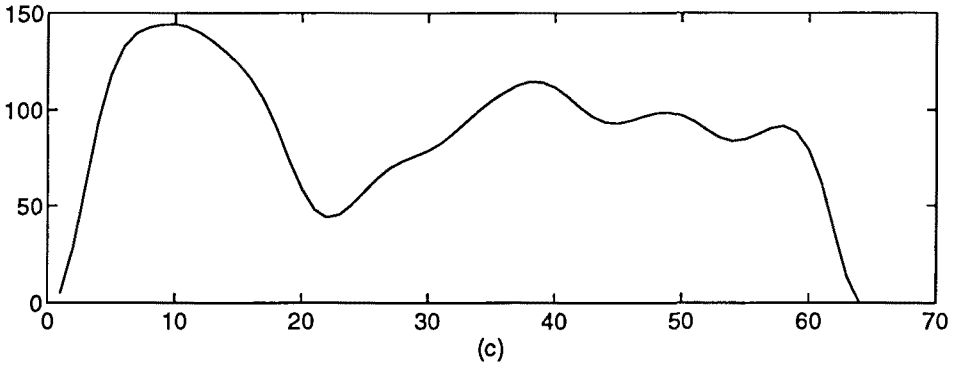
150
100
50
0
0
10
20
30
40
50
60
70
(c)

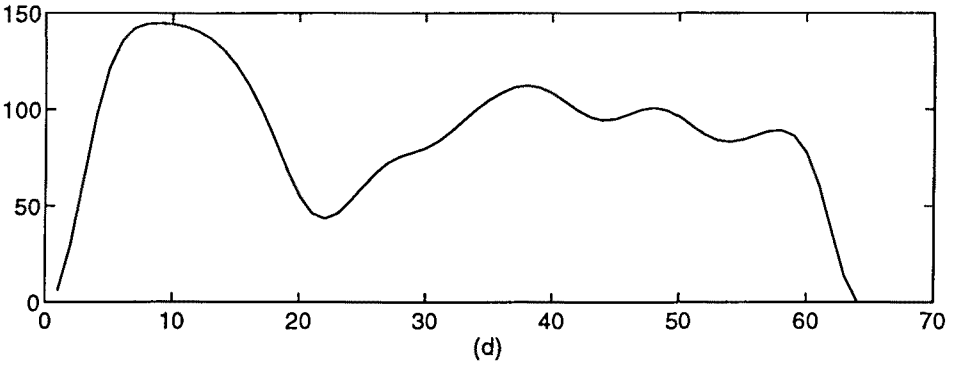
150
100
50
0
0
10
20
30
40
50
60
70
(d)

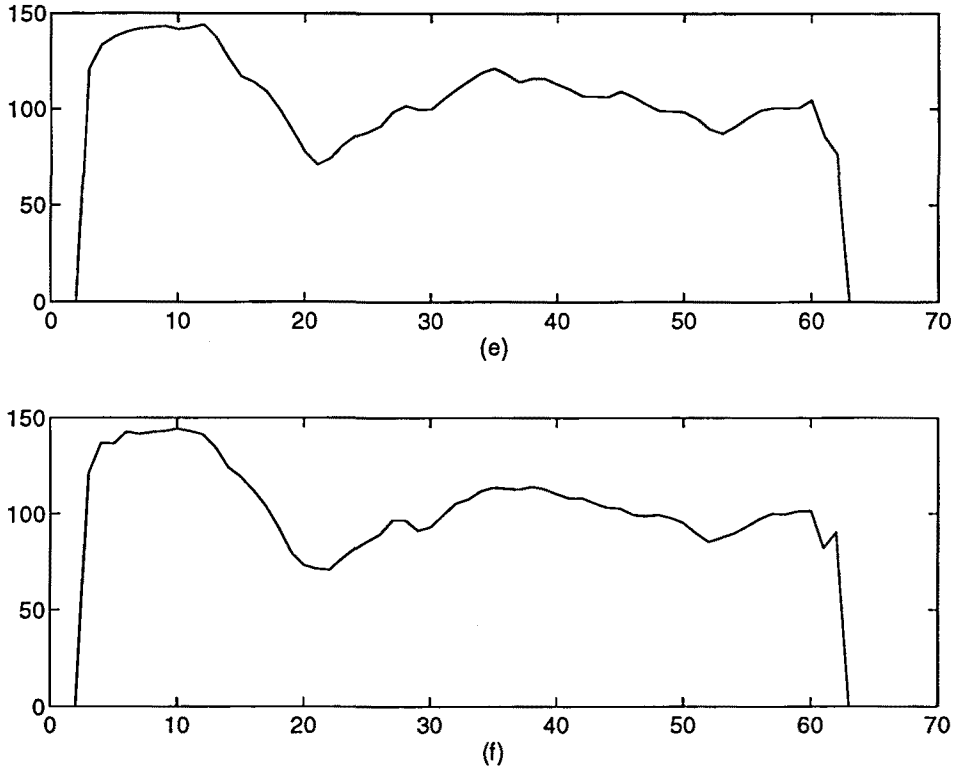

Fig. 3.13 (a) Original projection at angle 0 degrees. (b) Degraded projection, blurred by a 5x5 Gaussian filter, $\alpha = 0.9$, SNR = 5 dB. (c) Restored signal using parametric Wiener filter. (d) Restored signal using the magnitude of the Wiener filter and the true phase of the signal. (e) Restored signal using Algorithm 2. (f) Restored signal using Algorithm 3.

Example 5 : We can apply our method to restore the image of a blurred object moving in a noisy background. A translation in the 2-D image results in a shift in every projection except for one parallel to the direction of the shift. A rotation of the 2-D object results in a cyclic shift in the set of projection functions. Our test object is a pyramid object of dimensions 14x14 in a 64x64 image that has been convolved with a 5x5 Gaussian filter (α =0.35) . The translation of the object was simulated shifting the projections of the image. It was generated randomly with triangular distribution between +25 and -25. A total of 50 different images were employed with SNR of 25 dB. There was no rotation of the object. Fig. 3.14 (a) shows the original object, Fig. 3.14 (b) shows the blurred object, and finally Fig. 3.14 (c) shows the reconstructed object. Though we suppose known the dimensions of the blurring we do not know the dimensions of the object. The blurred-noisy object should be segmented just before applying the iterative phase reconstruction step in Algorithm 2.

Example 6 : We have simulated a sequence of short exposure speckle interferograms assuming Gaussian statistics for the atmosphere. Assuming that we know the dimensions of the object we uniquely reconstruct the third-order moment sequence from the phase of $\hat{B}_i(\omega_1,\omega_2)$ by means of Algorithm 3. Fig. 3.15 (a) shows a projection of a group of three simulated stars of different intensities. The image was diffracted through a rectangular pupil function. Fig. 3.15 (b) shows one of the 300 interferograms that were generated using Gaussian distribution for the real and imaginary part of $M(\omega)$ in Eq. (3.15). The reconstructed signal using Algorithm 2 is depicted in Fig. 3.15 (c) where we assumed that the length of the three stars was 16 samples. Fig. 3.16 (a) shows the third-order moment of the original projection whereas Fig. 3.16 (b) shows the average third-order moments computed from the interferograms. In Fig 3.16 (c) the third-order moment sequence of the object has been estimated through the iterative of Algorithm 3 using 2-D FFTs of sizes 256x256 with 150 iterations.

Fig. 3.17 (a) shows a projection of a group of two simulated stars. Fig. 3.17 (b) shows the reconstructed signal using Algorithm 3 from 300 speckle interferograms assuming a length equal to 8 samples. Fig 3.18 (a) presents the Bispectrum of the simulated double star and Fig. 3.18 (b) the Bispectrum we obtained dividing the average intensity Bispectrum and the Transfer function Bispectrum (computed from 300 observations of a point source). Fig. 3.18 (c) gives the estimated Bispectrum with 2-D FFTs of sizes 128x128 after 200 iterations.

Fig. 3.19 (a) shows the image of the 2 simulated stars. Fig. 3.19 (b) is one of the 300 speckle interferograms. Finally, Fig. 3.19 (c) shows the reconstructed image.

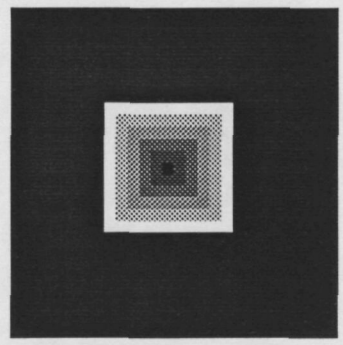

(a)

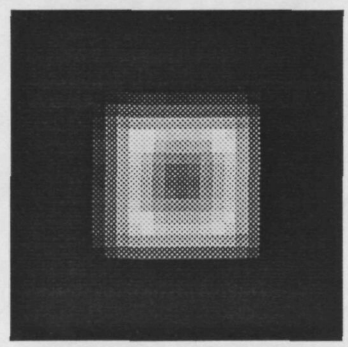

(b)

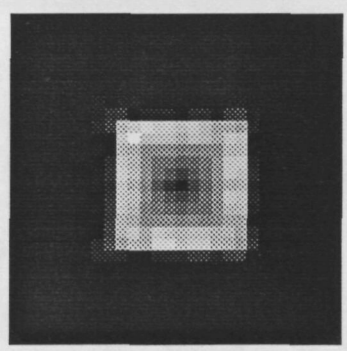

(c)

Fig. 3.14 (a) Original object of dimensions 14 x14 on a 64 x64 image. (b) One of the 50 observations of the object, blurred with 5x5 Gaussian filter, α = 0.35, SNR = 25 with random simulated translation of triangular distribution between 25 and -25. (c) Restored object using Algorithm 2.

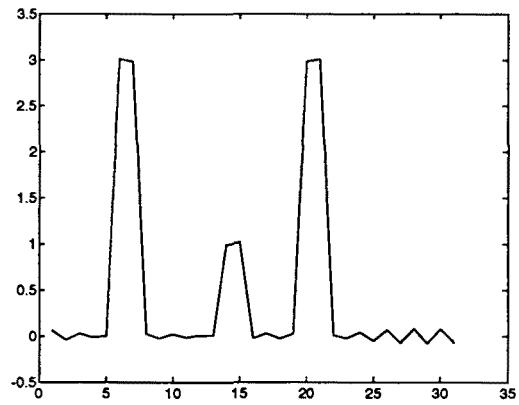

Fig. 3.15. (a) Projection of a diffracted image of three stars.

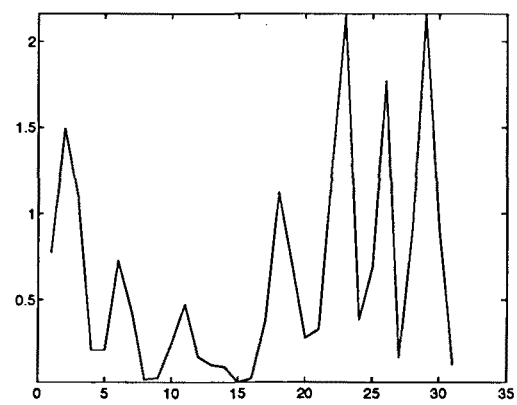

Fig. 3.15. (b) One of the 300 simulated speckle interferograms.

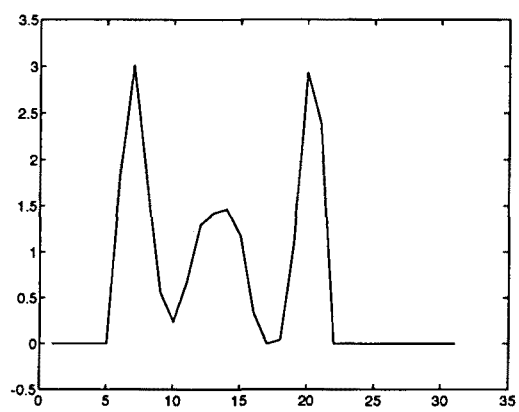

Fig. 3.15. (c) Solution from the reconstructed Bispectrum using Algorithm 2 and assuming length 16.

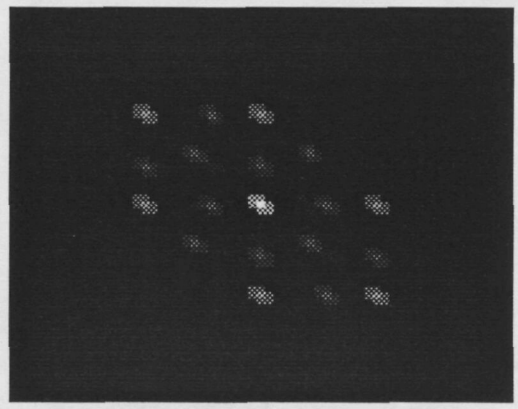

Fig. 3.16. (a) Third-order moment for the projection of Fig. 8 (a).

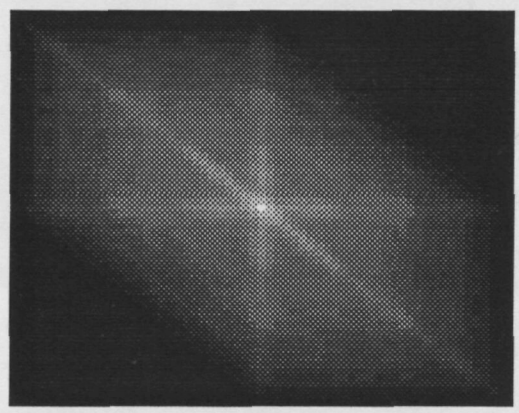

Fig. 3.16 (b) Average third-order moment interferogram.

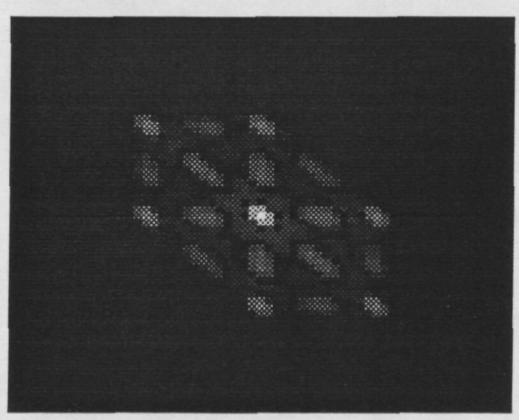

Fig. 3.16. (c) Reconstructed third-order moment from the iterative step in Algorithm 2.

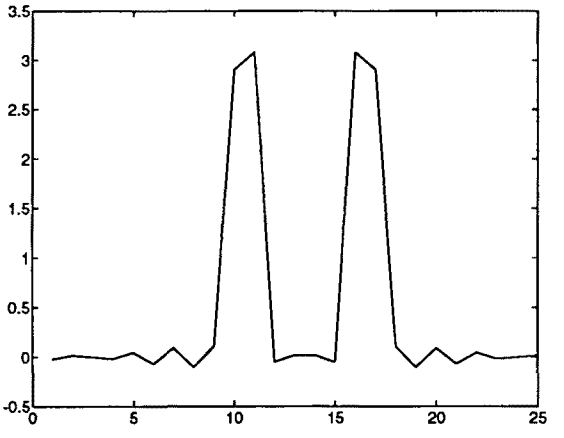

Fig. 3.17. (a) Projection of a diffracted image of two stars.

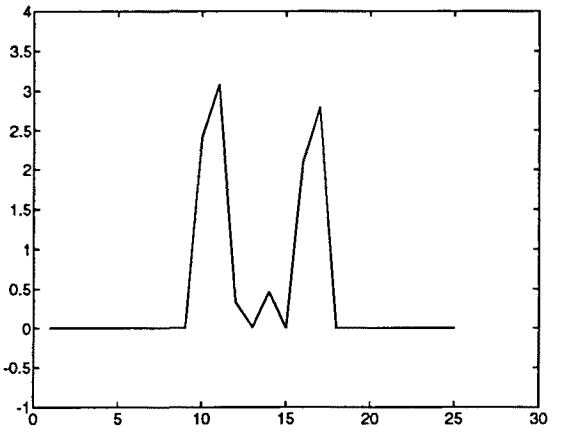

Fig. 3.17. (b) Solution from the reconstructed Bispectrum using Algorithm 2 and assuming length 8.

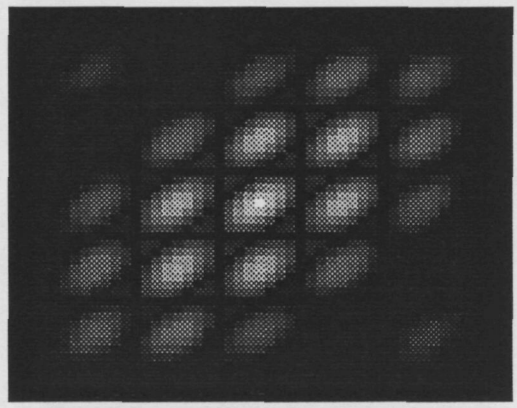

Fig. 3.18 (a) Bispectrum for the projection of Fig.3.18. (a).

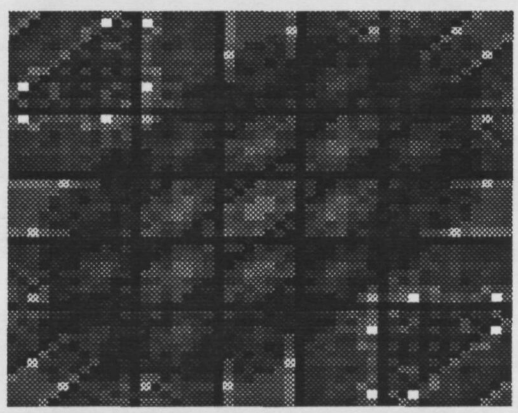

Fig. 3.18 (b) Division of $<B_i(\omega_1,\omega_2)>$ and $< B_p(\omega_1,\omega_2)>$, given 300 speckle interferograms

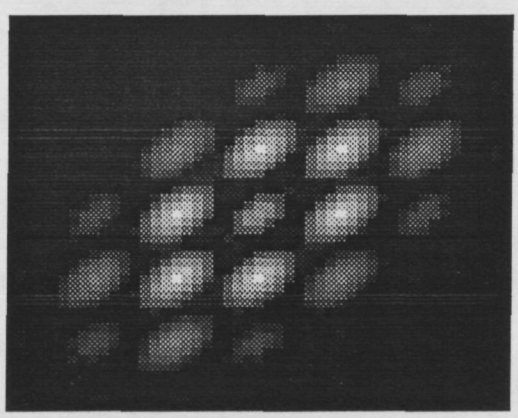

Fig. 3.18 (c) Estimated Bispectrum from the iterative step in Algorithm 2

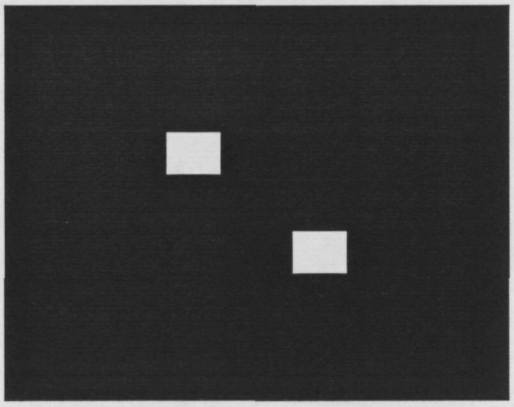

Fig. 3.19 (a) Simulated double star.

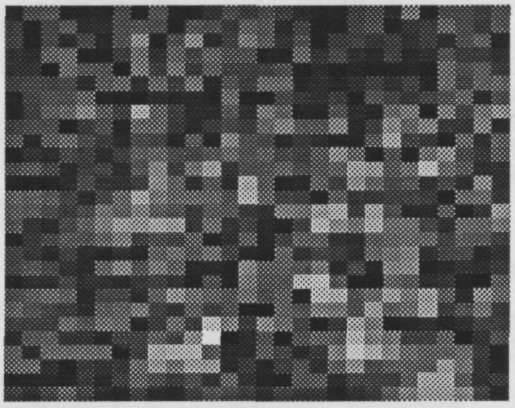

Fig. 3.19 (b) One of the 300 speckle interferograms

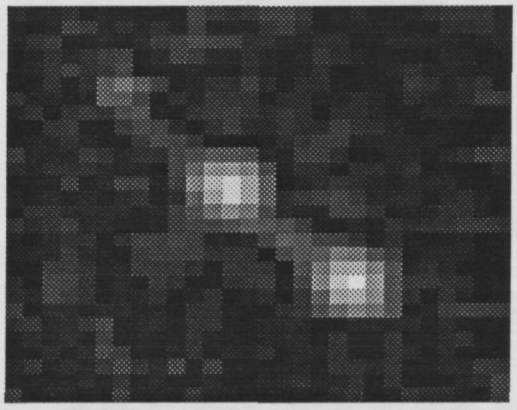

Fig.3.19 (c) Restored image using Algorithm 2.

Example 7 : In this example we apply Algorithm 3 to real astronomical images. They were provided by the Astrophysics Institute of Canaries and recorded from the "William Herschel" 4.2 m telescope at the Observatory of Roque de los Muchachos. Fig. 3.20 is one of the 300 speckle interferograms of size 256x256 that corresponds to a binary star separated 0,4 sec-arc (ADS4265). Fig. 3.21 (a) shows one of the projections at 0 degrees (vertical projection). Several choices for the length at this angle were given and found that the two stars were visible for length around 20 pixels. Algorithm 3 was employed using 2-D FFTs of sizes 512x512 with 25 iterations. The estimated projection is shown in Fig. 3.21 (b).

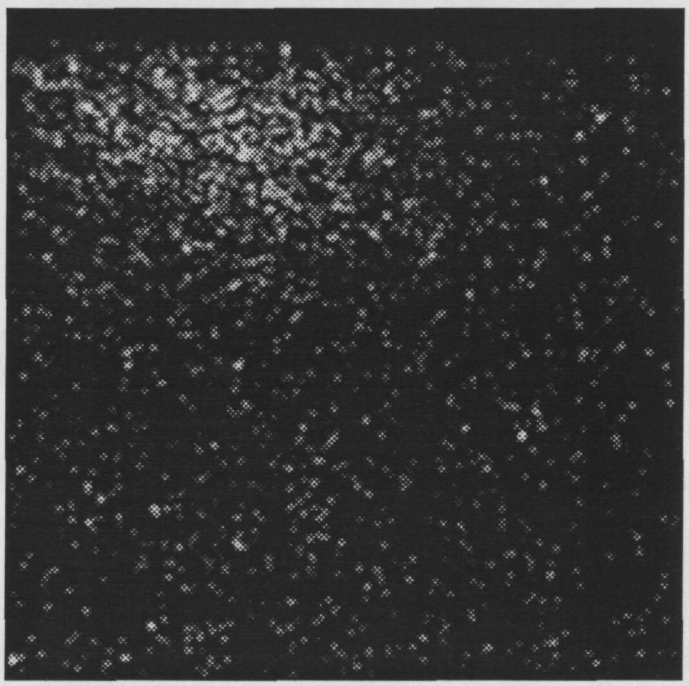

Fig. 3.20 One of the 300 real speckle interferograms.

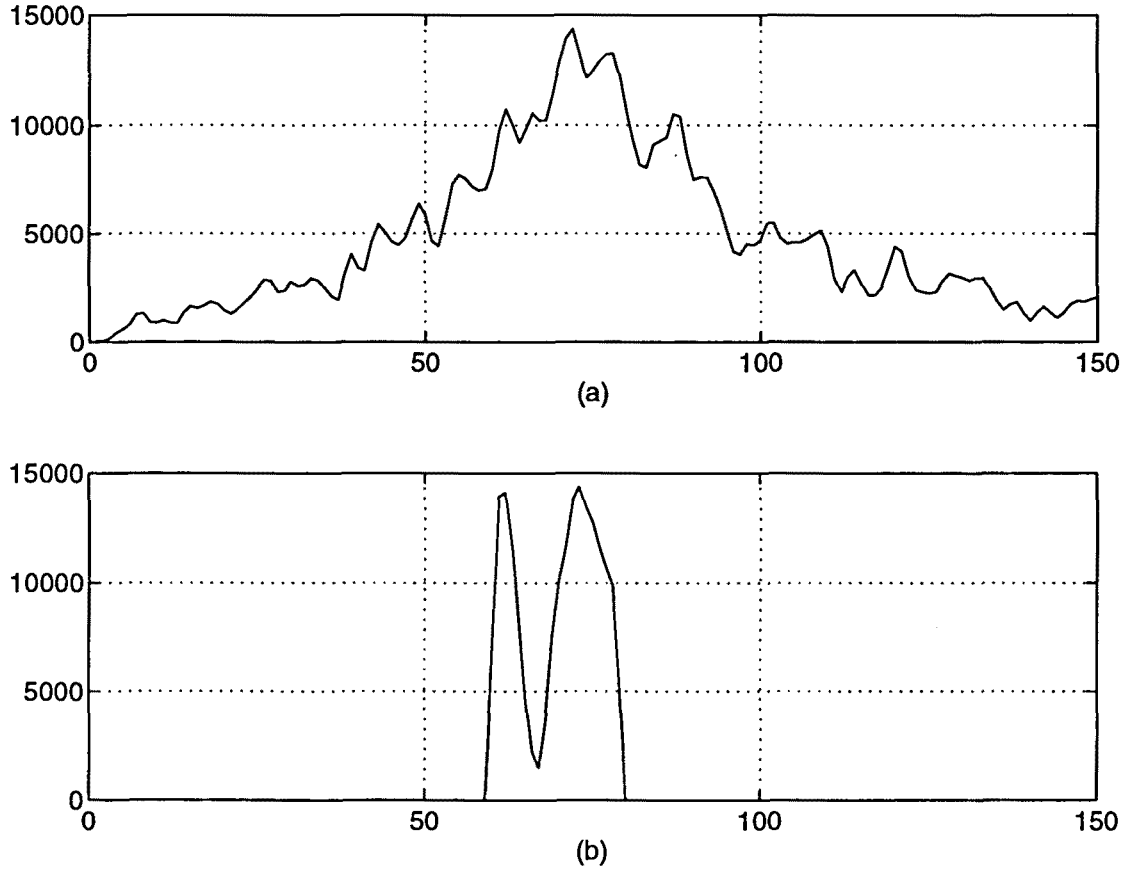

Fig. 3.21 (a) Projection at angle 0 from one of the 300 speckle interferograms . (b) Reconstructed projection using Algorithm 2.

3.4 Conclusions

In this chapter, we have shown that it is possible to restore degraded images from the HOS of its projections. Different restoration schemes were given to reconstruct the 1-D signals from either the phase of the Fourier Transform or the phase of the Bispectrum. They were applied to images distorted with deterministic PSF and Gaussian noise and to simulated and real astronomical images degraded by turbulent atmosphere of known statistics.

The motivation behind the use of these methods is the following. First, using HOS allows to reduce the effects of the noise and at the same time obtain an estimate of the Fourier phase or the Bispectrum phase of the signal that leads to the original signal. Second, employing the projections of the image reduces the high complexity associated with HOS of images. Theoretical bases have also been established to ensure the uniqueness of the reconstruction. Actually, this is the most interesting theoretical result obtained in this part of the thesis. Three HOS-based methods have been tested to carry out the reconstruction step. On one hand, we have seen that BIRA-based methods can be applied when we can ensure that the Z-Transform of the projections does not have zeros on the unit circle. On the other hand, the capability of the WS to reconstruct the projections from its third-order moments is demonstrated. Furthermore, for the case of deterministic PSF, the blurring filter was not used, only its size.

Although the complexity using HOS over 2-D signals is reduced, the computational load is still high. Nevertheless the quality of the images shown in this work was improved as compared to other existing methods. The results proved to be quite good for moderate SNR. For low SNR the restoration of the projections was also good, although small errors in some of the projections are easily propagated to the image.